# Impact of the Diurnal Radiation Cycle on Secondary Eyewall Formation

XIAODONG TANG, ZHE-MIN TAN, AND JUAN FANG

*Key Laboratory of Mesoscale Severe Weather, Ministry of Education, and School of Atmospheric Sciences, Nanjing University, Nanjing, China*

Y. QIANG SUN AND FUQING ZHANG

*Department of Meteorology, and Center for Advanced Data Assimilation and Predictability Techniques, The Pennsylvania State University, University Park, Pennsylvania*

(Manuscript received 19 January 2017, in final form 27 June 2017)

ABSTRACT

The sensitivity of the secondary eyewall formation (SEF) of Hurricane Edouard (2014) to the diurnal solar insolation cycle is examined with convection-permitting simulations. A control run with a real diurnal radiation cycle and a sensitivity experiment without solar insolation are conducted. In the control run, there is an area of relatively weak convection between the outer rainbands and the primary eyewall, that is, a moat region. This area is highly sensitive to solar shortwave radiative heating, mostly in the mid- to upper levels in the daytime, which leads to a net stabilization effect and suppresses convective development. Moreover, the heated surface air weakens the wind-induced surface heat exchange (WISHE) feedback between the surface fluxes (that promote convection) and convective heating (that feeds into the secondary circulation and then the tangential wind). Consequently, a typical SEF with a clear moat follows. In the sensitivity experiment, in contrast, net radiative cooling leads to persistent active inner rainbands between the primary eyewall and outer rainbands, and these, along with the absence of the rapid filamentation zone, are detrimental to moat formation and thus to SEF. Sawyer–Eliassen diagnoses further suggest that the radiation-induced difference in diabatic heating is more important than the vortex wind structure for moat formation and SEF. These results suggest that the SEF is highly sensitive to solar insolation.

## 1. Introduction

Secondary eyewalls in tropical cyclones (TCs) have been well documented from radar and satellite imagery (e.g., Willoughby et al. 1982; Houze et al. 2007; Kossin and Sitkowski 2009; Kuo et al. 2009; Hence and Houze 2012; Abarca et al. 2016). They are identified as a secondary deep convective ring associated with a secondary maximum tangential wind outside the primary eyewall with a nearly cloud-free region (moat) between the two concentric eyewalls. Secondary eyewall formation (SEF) is a key issue for TC research and forecasting, as it is closely related to both short-term TC intensity change (e.g., Houze et al. 2007; Yang et al. 2013) and TC size change (Maclay et al. 2008).

Several mechanisms for SEF have been proposed and frequently discussed, including 1) vortex Rossby wave radiation and the associated wave–mean flow interaction near the critical radius (Montgomery and Kallenbach 1997; Qiu et al. 2010; Abarca and Corbosiero 2011; Menelaou et al. 2012); 2) axisymmetrization leading to vorticity ring formation outside of the primary eyewall (Kuo et al. 2004, 2008); 3) beta-skirt axisymmetrization in a region with sufficiently long filamentation time and moist convective potential, together with a follow-up wind-induced surface heat exchange (WISHE) process (Terwey and Montgomery 2008; Qiu et al. 2010); 4) unbalanced dynamics associated with the TC boundary layer (BL) (Huang et al. 2012; Abarca and Montgomery 2013; Wang et al. 2013); 5) axisymmetrization and balanced response to latent heating from the outer rainbands in a region of enhanced inertial stability outside the primary eyewall

Denotes content that is immediately available upon publication as open access.

*Corresponding author*: Xiaodong Tang, xdtang@nju.edu.cn

DOI: 10.1175/JAS-D-17-0020.1

(Fang and Zhang 2012; Rozoff et al. 2012; Sun et al. 2013; Zhang et al. 2017); and 6) positive feedback among local enhancement of the radial vorticity gradient, BL frictional updraft, and convection (Kepert 2013; Kepert and Nolan 2014; Zhang et al. 2017).

Although there is no clear consensus so far on the fundamental physics that fully explains the SEF process (Wu et al. 2016), it is recognized that the outer rainbands might play a critical role for SEF in most of the proposed mechanisms (Qiu and Tan 2013; Sun et al. 2013; Zhang et al. 2017). Inner rainbands are spirally banded structures related to vortex Rossby waves within about 3 times the radius of maximum wind (RMW) from the hurricane center, according to the predominant view (e.g., Montgomery and Kallenbach 1997; Wang 2009). Outer rainbands are located outside the inner core. Qiu and Tan (2013) showed that asymmetric BL inflow induced by the outer rainbands could penetrate the inner-core region, reinforce convergence at the leading edge of the strong inflow, and lift the moist and warm air in this region continuously, which would contribute to the SEF. Moreover, Judt and Chen (2010) suggested that a higher rate of potential vorticity (PV) generation and accumulation in the outer rainbands region could lead to SEF. The diabatic heating resulting from convective and stratiform precipitation in the outer rainbands can also induce a secondary wind maximum (Moon and Nolan 2010). It has been further argued that diabatic heating generated by convection in the outer rainbands must reach a critical strength relative to that of the eyewall convection, in order to initiate SEF (Zhu and Zhu 2014). In addition, Fang and Zhang (2012) found that the initiation and organization of the outer rainbands preceding SEF might be facilitated by a front-like feature in the low-level equivalent potential temperature field and a slow filamentation zone near the extensive stratiform region.

In our previous paper on this topic (Tang and Zhang 2016, hereafter TZ16), we demonstrated the impacts of radiation on the size and strength of the mature Hurricane Edouard (2014). We also reported a clear SEF in a control run (see Fig. 8a in TZ16), consistent with observations (Fig. 1; Abarca et al. 2016; Braun et al. 2016). There is no apparent SEF and eyewall replacement cycle (ERC) in the sensitivity experiment with no solar insolation (i.e., experiment NoSolarRad72h; see Fig. 8b in TZ16), suggesting that SEF is highly sensitive to solar shortwave radiation. However, the mechanism by which the solar insolation affects SEF remains unexplored, and this is the focus of the current study.

The remainder of this paper is organized as follows. Section 2 provides a brief review of the model settings and experimental design of the control and sensitivity experiments. Section 3 gives an overview of the evolution of Hurricane Edouard (2014) focusing on SEF and ERC in the observations and model simulations. Section 4 discusses the impacts of radiative forcing on moat formation, development of the outer rainbands, and the BL processes preceding SEF. The possible mechanism behind the sensitivity of the SEF to solar radiation is also proposed. Finally, concluding remarks are given in section 5.

## 2. Model settings and experimental design

As described by TZ16, the Advanced Research version of the WRF Model (ARW, version 3.5.1) was employed to perform a control simulation (CNTL) and sensitivity experiments, using three nested domains. The horizontal grid spacing and coverage are 27 km and 379 × 244, 9 km and 298 × 298, and 3 km and 298 × 298 for the first (D01), second (D02), and third (D03) domains, respectively. All three domains are run with 43 terrain-following eta levels in the vertical with model top at 10 hPa. The Dudhia shortwave radiation scheme (Dudhia 1989), the Rapid Radiation Transfer Model (RRTM) longwave radiative scheme (Mlawer et al. 1997), the WRF single-moment 6-class microphysics scheme (Hong and Lim 2006), and the Yonsei University (YSU) scheme for the planetary BL (Hong et al. 2006) are employed for all domains. Cumulus convection is parameterized using the Grell–Freitas cumulus scheme (Grell and Freitas 2014) and is applied only in D01.

CNTL is initialized with the composite initial conditions from the 10 best-performing members, produced by the Pennsylvania State University (PSU) real-time WRF ensemble Kalman filter (WRF–EnKF) analysis and forecast system (Zhang and Weng 2015; Weng and Zhang 2016; Munsell et al. 2017), and is then integrated from 1200 UTC 11 September for 168 h using the GFS analysis as the boundary conditions at the outermost grid. To elucidate the effects of solar insolation on the SEF of Hurricane Edouard (2014), a sensitivity experiment named "NoSolarRad" is conducted with no solar insolation, starting at 72 model integration hours of the control simulation (the NoSolarRad72h experiment in TZ16, their Table 1), which is about 2 days before SEF in the CNTL experiment.

## 3. Overview of the SEF and ERC of Hurricane Edouard (2014)

Hurricane Edouard (2014) occurred during the 2014 phase of the Hurricane and Severe Storm Sentinel

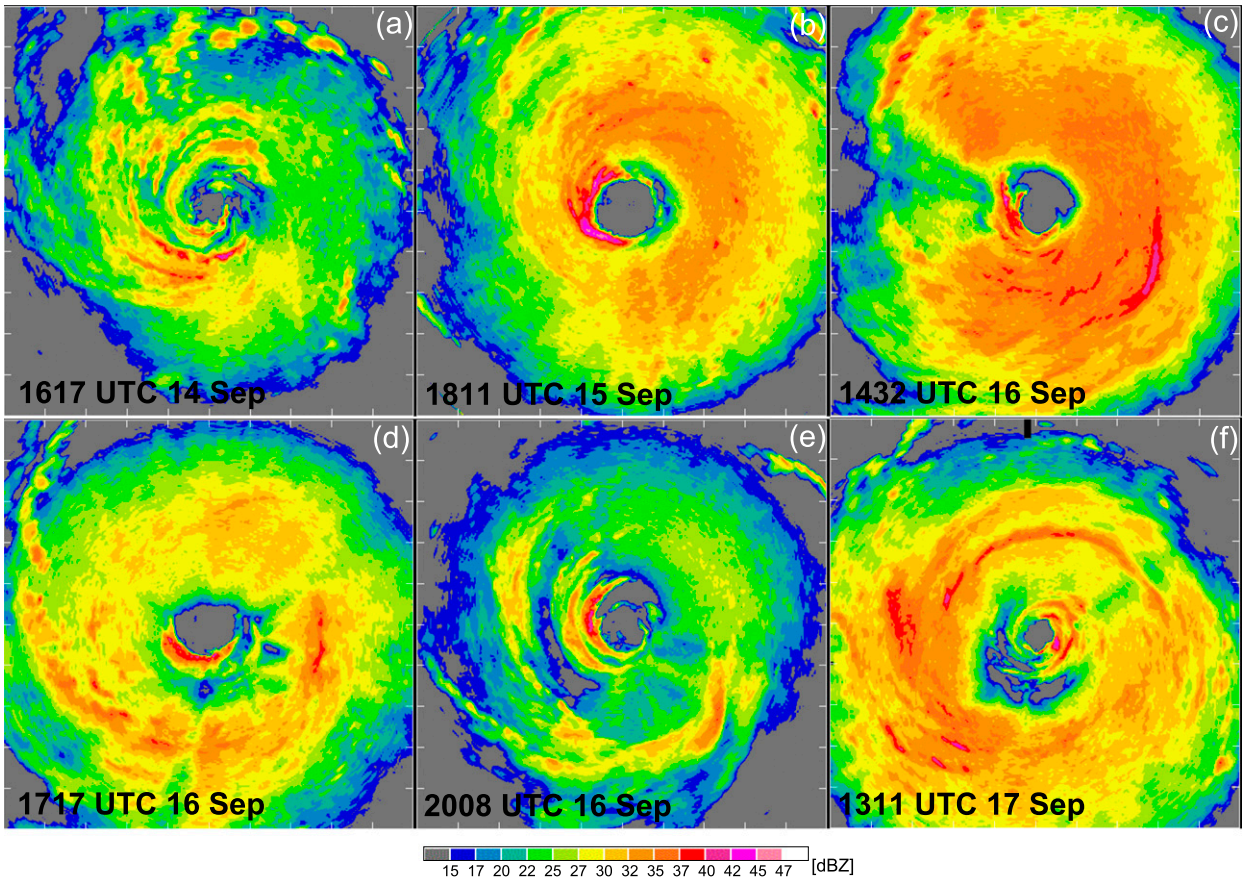


FIG. 1. Composite radar reflectivity (shading; dB$Z$) over a 360 km × 360 km square region from aircraft reconnaissance into Hurricane Edouard from 1617 UTC 14 Sep to 1311 UTC 17 Sep 2014: (a) 1617 UTC 14 Sep, (b) 1811 UTC 15 Sep, (c) 1432 UTC 16 Sep, (d) 1717 UTC 16 Sep, (e) 2008 UTC 16 Sep, and (f) 1311 UTC 17 Sep. Courtesy of the NOAA/AMOL/Hurricane Research Division (http://www.aoml.noaa.gov/hrd/Storm_pages/edouard2014/radar.html).

(HS3) experiment (Braun et al. 2016) and Intensity Forecasting Experiment (IFEX; Rogers et al. 2013). Abundant in situ and aircraft observations were collected during its life cycle and can be used to address questions about the SEF processes in hurricanes and the forecast skill of our forecast system for events of this type (Munsell et al. 2017). The concentric eyewall structure of Edouard and its evolution are evident in aircraft-based radar reflectivity composites generated by the NOAA Hurricane Research Division of the AOML (Fig. 1). The SEF in Hurricane Edouard occurred approximately during the period from 1600 to 1800 UTC 16 September (Fig. 1d), and the follow-up ERC was completed with the erosion of inner-core convection during the period from 1300 to 1600 UTC 17 September (Fig. 1f), consistent with other studies (e.g., Stewart 2014; Abarca et al. 2016). Our simulation in CNTL also successfully captured the SEF and ERC processes (Figs. 2, 3). Figure 2 shows snapshots of the synthetic radar reflectivity at 5 km in our CNTL experiment. The tangential and radial winds (Figs. 4a–c), along with the vertical velocity (Figs. 5a,b), are also plotted. In terms of the azimuthally averaged tangential wind at the 1-km level, the ERC in CNTL showed that the secondary eyewall in the simulated Edouard formed around 1800 UTC 16 September and the eyewall replacement was completed with the loss of the tangential wind speed inside the secondary eyewall at ~0900 UTC 17 September (Fig. 4a).

Before the SEF, the simulated Edouard (2014) underwent a rapid intensification process from 1200 UTC 14 September to 1200 UTC 15 September (Fig. 1b in TZ16). The 1-km maximum azimuthal-mean tangential wind increased from 26 to 54 m s$^{-1}$ with contraction of the RMW from ~50 to ~35 km during this 24-h period in CNTL. Subsequently, the maximum azimuthal-mean tangential wind slowly increased and reached its peak intensity of 70 m s$^{-1}$ at ~0600 UTC 16 September, while the RMW remained at ~36 km (Fig. 4a). The maximum low-level azimuthal-mean radial inflow at 1 km and outflow at 2 km in CNTL are located close to the RMW before the SEF (Figs. 4b,c).

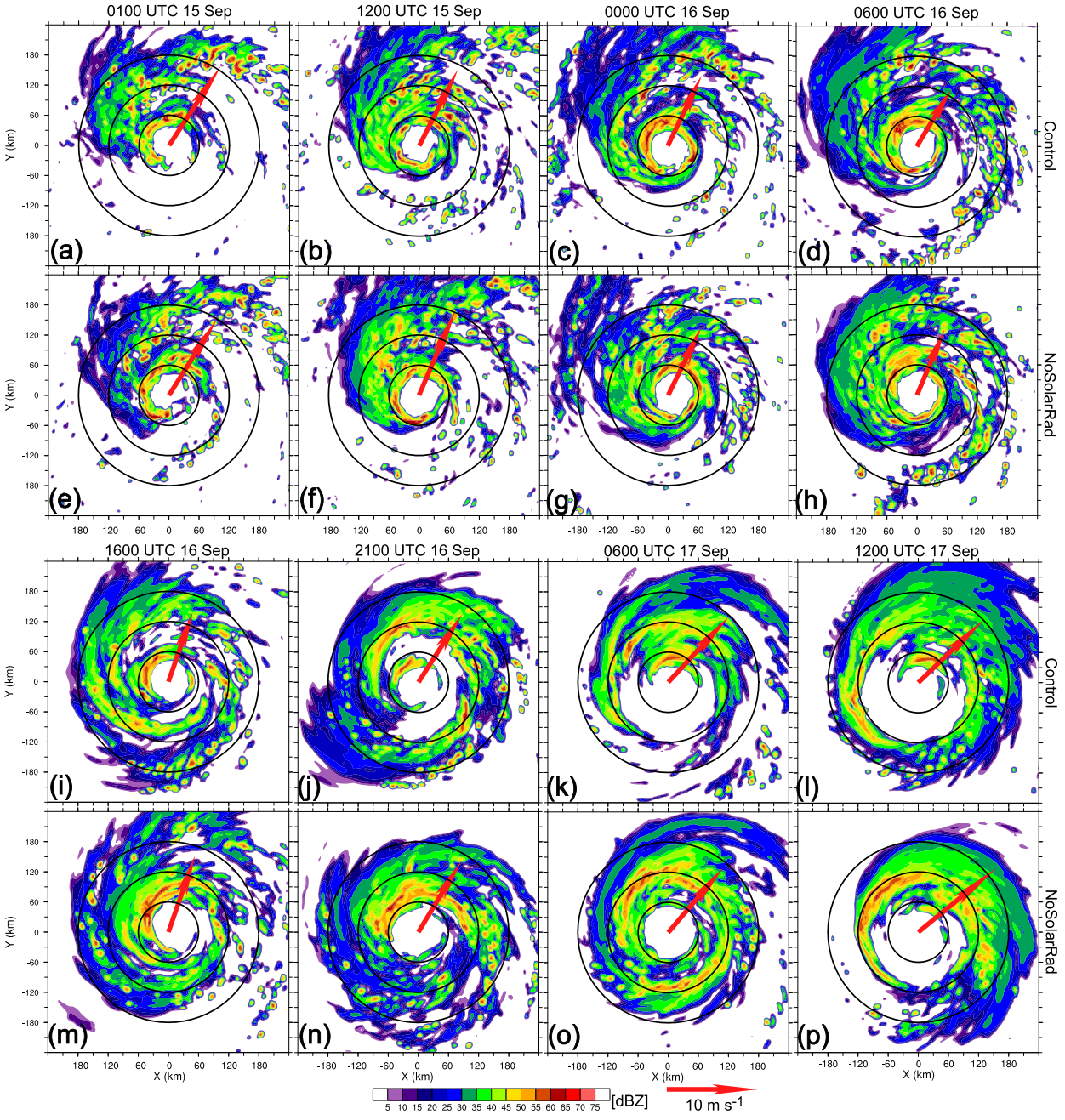


FIG. 2. Snapshots of synthetic radar reflectivity (dB$Z$) at a height of 5 km and vertical shear vectors of averaged environmental wind (red arrows) for (a)–(d),(i)–(l) CNTL and (e)–(h),(m)–(p) NoSolarRad. The circles are centered over the storm center with radii of 60, 120, and 180 km.

In comparison with CNTL, in NoSolarRad the maximum radial inflow was farther out from the RMW during the period from 1800 UTC 15 September to 0600 UTC 16 September (Fig. 4e), and the maximum of the 2-km outflow in NoSolarRad started to broaden radially at ~0600 UTC 16 September, without a continuous secondary maximum (Fig. 4f). The inner and outer rainband regions in the study (Figs. 2, 3) are identified at radii between 60 and 90 km and beyond 90 km, respectively, according to their definitions in section 1. The latent heat release from the stronger convective activities in the inner rainbands outside the primary eyewall in NoSolarRad prevents the low-level inflow from penetrating as far into the primary eyewall as in CNTL.

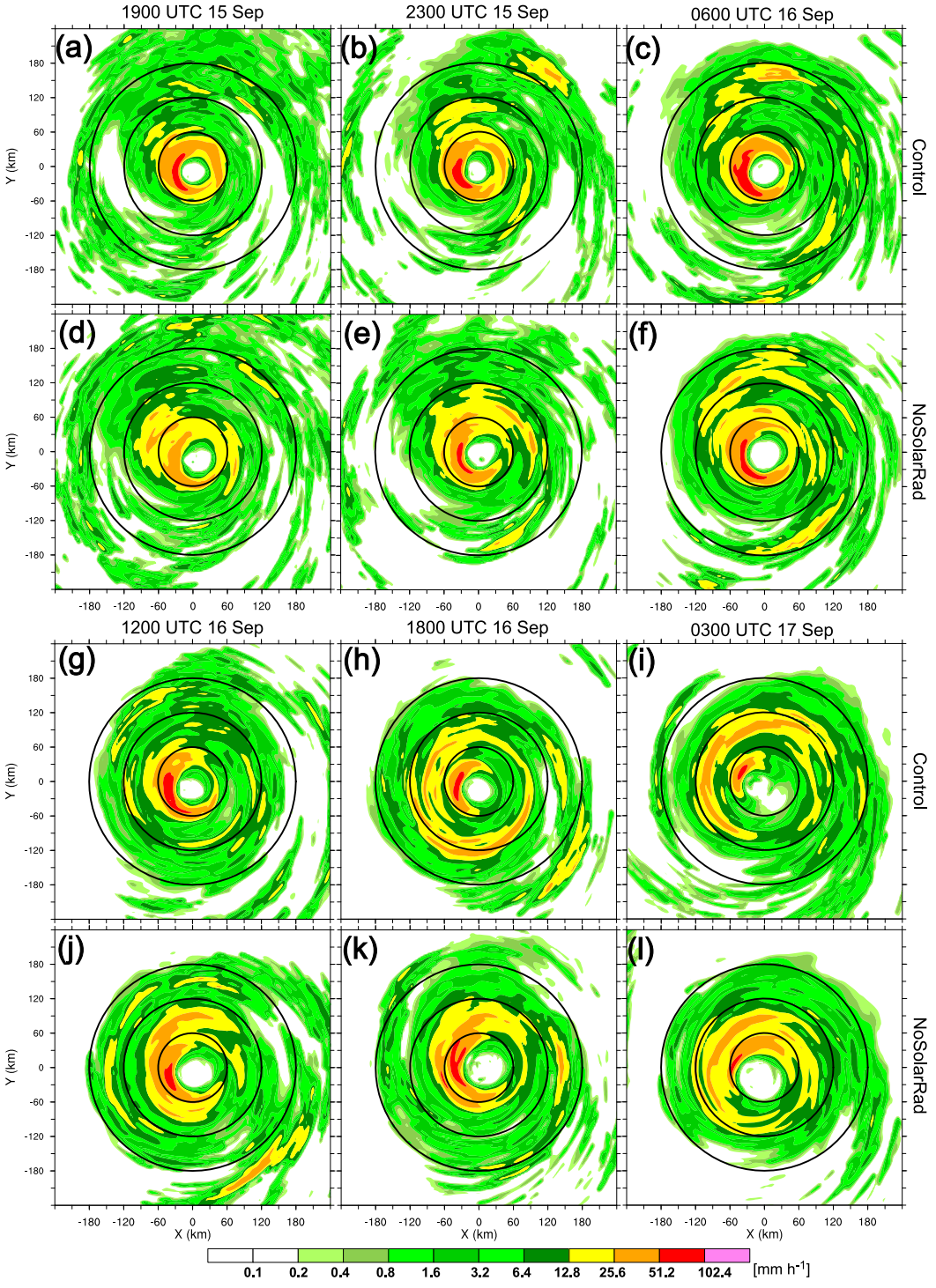


FIG. 3. Snapshots of surface rainfall rate (mm $h^{-1}$) for (a)–(c),(g)–(i) CNTL and (d)–(f),(j)–(l) NoSolarRad. The circles are centered over the storm center with radii of 60, 120, and 180 km.

This then leads to more (less) convergence outside (at) the primary eyewall (Figs. 3, 5a–d), suggested by TZ16. The RMW in NoSolarRad also began to move outward slowly after ~0000 UTC 16 September (Fig. 4d) due to stronger diabatic heating from the inner rainbands (Figs. 2, 3f, 3j–l, 5c, 5d, 6d).

After 0000 UTC 16 September, upward motion in the outer core (outside 150 km radial distance) at the

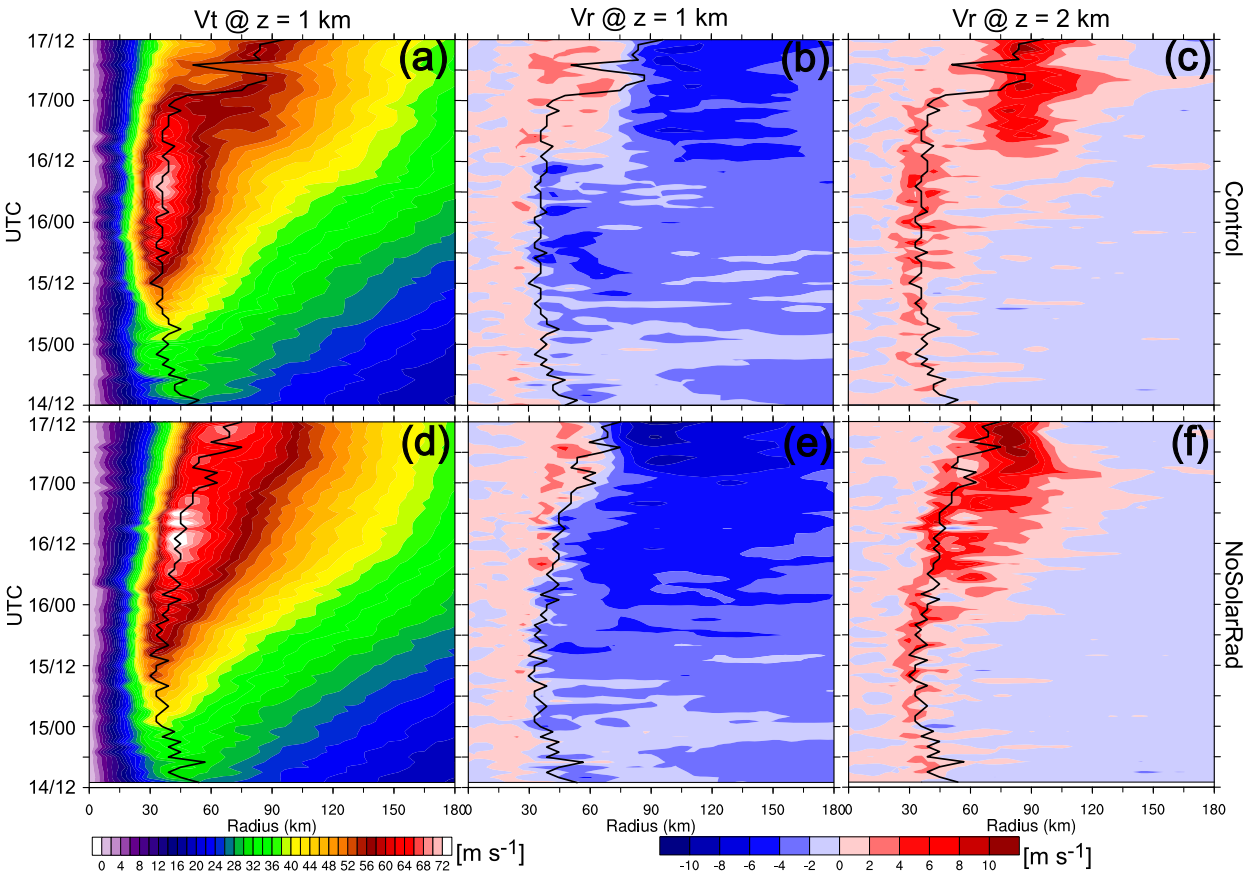


FIG. 4. Hovmöller plots of azimuthal-mean tangential velocity at a height of 1 km and radial velocity at heights of 1 and 2 km for (a)–(c) CNTL and (d)–(f) NoSolarRad. The superposed black lines denote the RMW at 1 km.

midlevel in CNTL became more organized, and began to move inward and then connected with the lower-layer updraft ejected from the top of the BL [i.e., the height of zero inflow as defined by Smith et al. (2009); Figs. 5a,b], as shown in the next section. Figures 2c and 2d suggest that the upward motion is associated with the formation and organization of the outer rainbands. The double maximum inflow regions at the 1-km level and the corresponding double maximum outflow at the top of BL formed at ~1200 UTC 16 September (Figs. 4b,c). Meanwhile, the outer tangential wind field expanded rapidly (Fig. 4a), which has been suggested as a precursor of SEF (Huang et al. 2012; Rozoff et al. 2012; Wang et al. 2016). There is a clear moat region with little upward motion from low (2 km) to middle levels (6 km) at this time in CNTL (Figs. 5a,b), while the secondary maximum of the tangential winds associated with the secondary eyewall formed 6 h later (Fig. 4a). The ERC was completed at ~1200 UTC 17 September with the collapse of the inner eyewall (Figs. 2l, 4a–c).

In NoSolarRad, moist convection was more active than in CNTL in the region outside the eyewall (60–120 km) until 0200 UTC 17 September, connecting the primary eyewall and the outer rainbands (Figs. 2e–h, 2m, 2n, 3d–f, 3j–l, 5c, 5d). Consequently, there was no space for clear moat formation in NoSolarRad. The continuous latent heat release from the active inner rainbands outside the eyewall resulted in enhanced low-level inflow over this region without a clear gap (Fig. 4e; Fudeyasu and Wang 2011; Rozoff et al. 2012). Latent heating outside the RMW also increased (reduced) low-level tangential wind outside (inside) the RMW and led to the expansion of the RMW (Shapiro and Willoughby 1982). This persistent yet slow expansion of the RMW (Fig. 4d) and the associated eyewall convection (Figs. 5c,d) prevented an abrupt broadening of the tangential wind as in CNTL (cf. Figs. 4a and 4d) and the follow-up SEF. Instead, the size of the cyclone increased gradually in NoSolarRad.

As mentioned above, the critical differences between CNTL and NoSolarRad are the stronger inner rainbands and the lack of a clear moat region in NoSolarRad. Next we consider the role of the diurnal solar radiation in this process and how it inhibits SEF in NoSolarRad but favors SEF in CNTL.

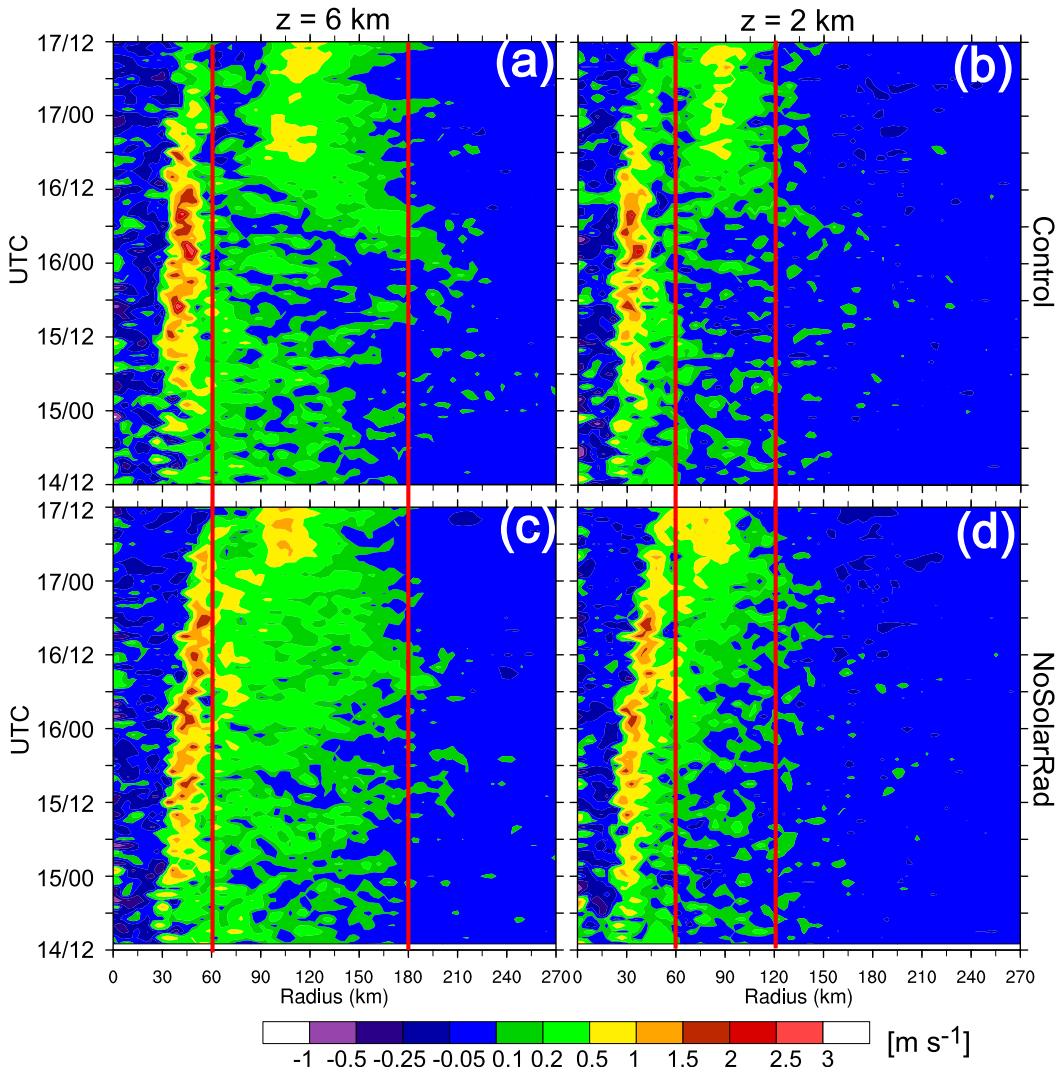


FIG. 5. Hovmöller plots of azimuthal-mean vertical velocity at heights of 6 and 2 km for (a),(b) CNTL and (c),(d) NoSolarRad. The vertical red lines show key radial distances.

## 4. Radiative effects on SEF

The influence of solar radiation on the moat, and on the formation and development of rainbands is investigated by comparing experiments with (CNTL) and without (NoSolarRad) solar radiation. Figure 2 plots the vertical wind shear (VWS) using the data from D02 of the WRF simulations. This is defined as the difference in the averaged environmental wind vectors for the annulus with radii of 200 and 800 km surrounding the storm center between the heights of 12 and 1.5 km, as in Zehr (2003). The results show that before 1200 UTC 17 September, the differences in VWS magnitude and direction between the CNTL and NoSolarRad are less than 1 m s$^{-1}$ and 10°, respectively. Although the VWS plays an important role in the asymmetric distribution of convection within the rainbands, the solar insolation effect on VWS may be ignored, given such small differences between the VWS in CNTL and NoSolarRad. The pathway by which radiative effects act on SEF is discussed below.

### *a. Moat formation*

A clear moat formed in CNTL within the radial range of 60–75 km, accompanied by the secondary eyewall outside the moat (Figs. 2i, 2j, 3h, 3i, 4a, 4b) after 1200 UTC 16 September, as observed (Fig. 1e). Figure 6 shows the radiative heating differences between CNTL and NoSolarRad averaged over the moat region before the SEF. The net radiative heating in CNTL is much stronger than that in NoSolarRad throughout the troposphere due to daytime solar insolation, especially at

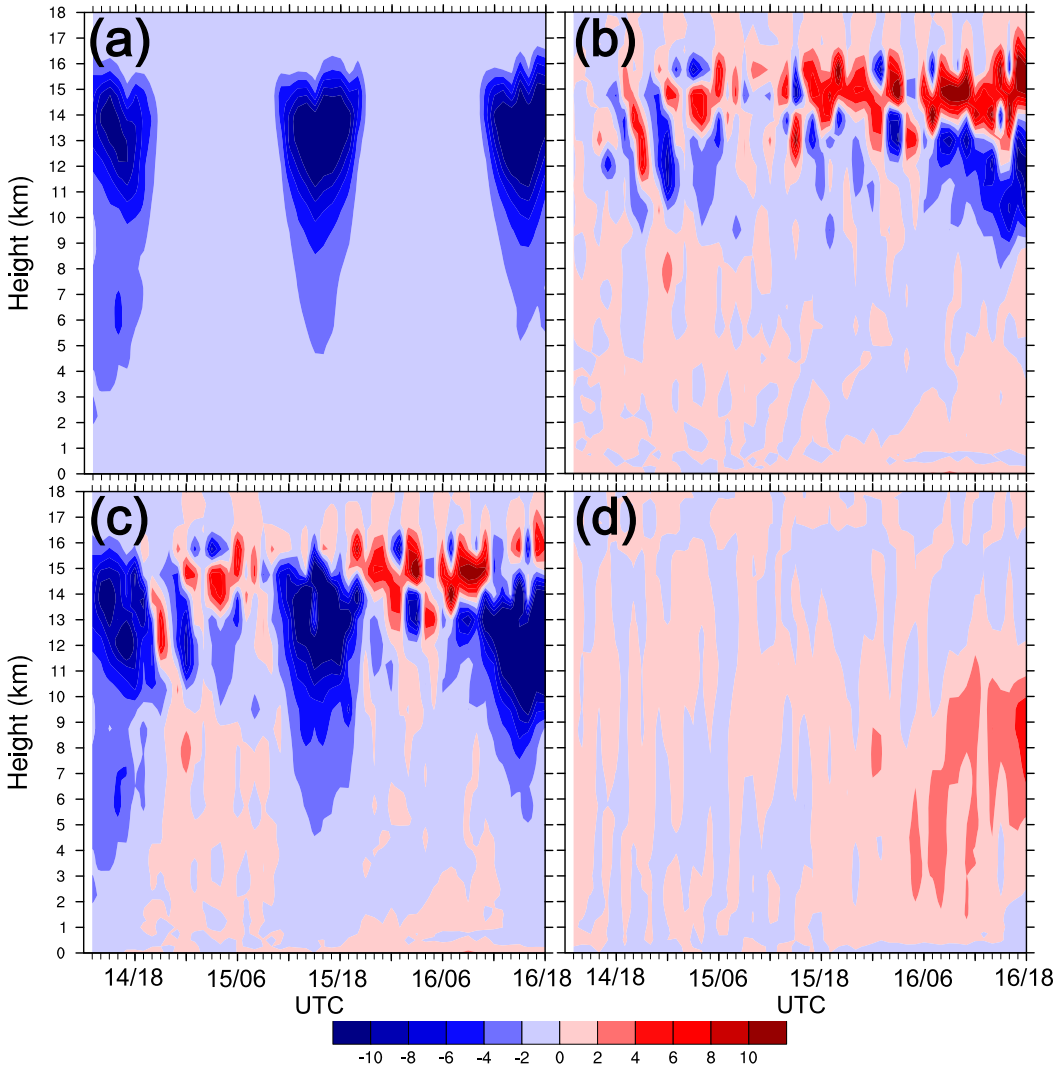


FIG. 6. Height–time plot of NoSolarRad minus CNTL difference of (a) shortwave radiative heating, (b) longwave radiative heating, (c) net radiative heating, and (d) latent heating averaged between 60- and 75-km radius from 1300 UTC 14 Sep to 1800 UTC 16 Sep 2014. The units are $10^{-5}$ K s$^{-1}$ for (a)–(c) and $10^{-3}$ K s$^{-1}$ for (d).

upper levels (11–14 km; Figs. 6a–c). The magnitude of the differences in net radiative heating during the daytime is 0.5–1 K day$^{-1}$ at the top of the BL, and over 10 K day$^{-1}$ at upper levels. Although net radiative cooling at nighttime offsets the radiative heating at daytime in CNTL, the 2-day-averaged results also show greater net radiative heating in the CNTL compared with the NoSolarRad (figure not shown). While warmer upper levels are present in a wide radial range from the storm center to outer core (cf. TZ16), they further reduce the likelihood of deep moist convection (Fig. 5), together with the weaker low-level convective instability in the moat region (Figs. 9a,b,e,f). This is consistent with the finding in TZ16. The greater radiative heating also results in greater near-surface air temperature after 1 day due to clearer sky in CNTL than in NoSolarRad (Fig. 7a), which induces a further decrease in the temperature gradient at the air–sea interface and the surface sensible heat flux for a given sea surface temperature compared with NoSolarRad (Fig. 7e). While the energy input from the sea surface (i.e., surface latent heat and sensible heat fluxes) was weaker in CNTL, the most unstable convective available potential energy (MCAPE[1]) was larger (Figs. 7b,d,e), indicating less consumption of CAPE and thus less convective activity in the moat region of CNTL than of NoSolarRad (Li and

[1] MCAPE is calculated for a parcel with the highest equivalent potential temperature below 3000 m AGL.

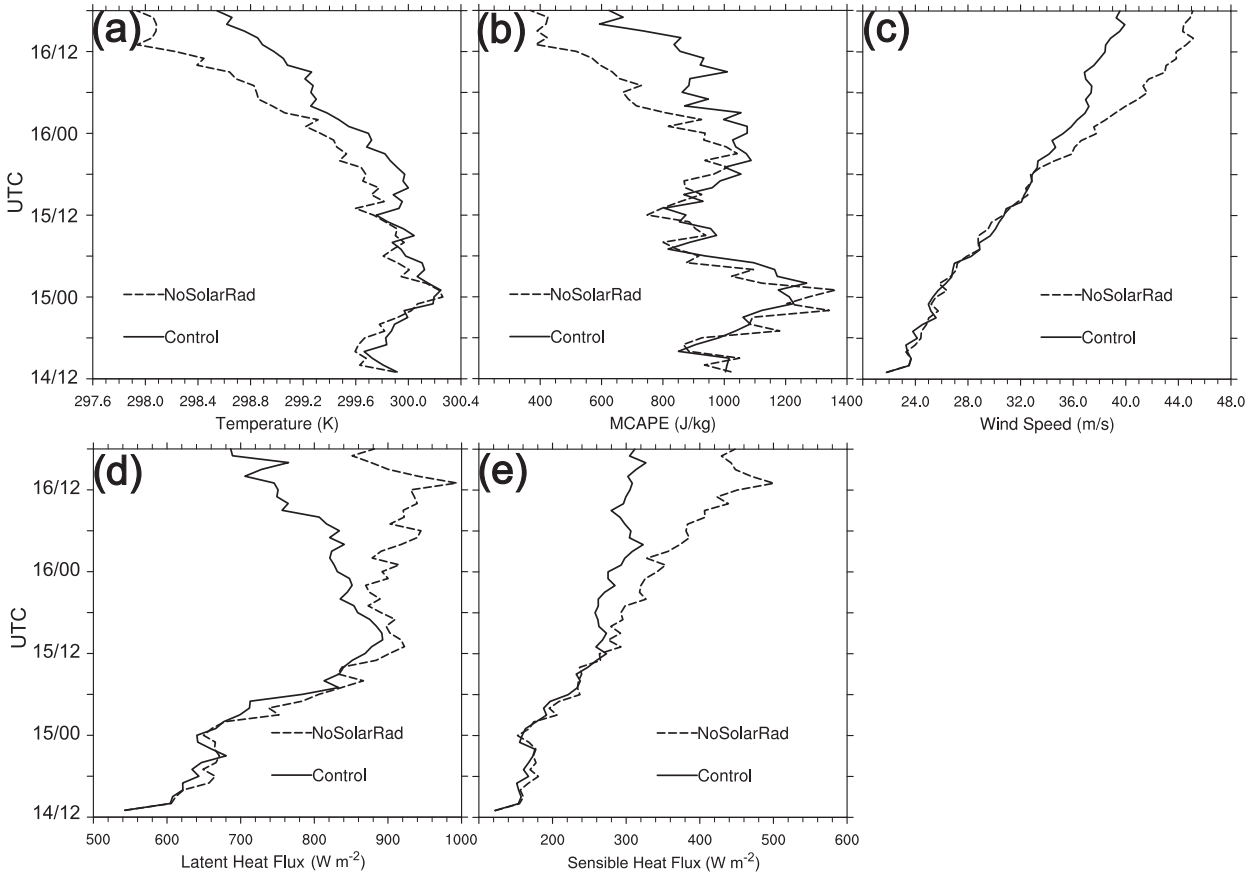


FIG. 7. Evolution of (a) 2-m temperature, (b) MCAPE, (c) 10-m wind speed, and surface fluxes of (d) latent heat and (e) sensible heat averaged between 60- and 75-km radius for CNTL and NoSolarRad.

Wang 2012; Melhauser and Zhang 2014). Less diabatic heating due to suppressed convection in CNTL (Fig. 6d) also leads to weaker surface winds (Fig. 7c) and hence weaker surface fluxes of latent heat and sensible heat (Figs. 7d,e). As a result, the convection is further suppressed, facilitating moat formation in CNTL. Surface friction will increase with increasing surface wind speed and retard it to a certain extent, so the deviation of latent heat and sensible heat fluxes between CNTL and NoSolarRad precedes that of surface wind speed (cf. Figs. 7c–e). Consequently, the impact of the difference in air–sea interface temperature and moisture gradient on surface heat fluxes also precedes that of the surface wind speed difference. In contrast, in NoSolarRad an enhanced positive feedback among surface fluxes, inner rainband convection, and the acceleration of tangential wind at low levels through the WISHE mechanism (Emanuel 1986) reduces the possibility of moat formation (Figs. 3d–f, 3j–l, 4d, 4e, 5c, 5d, 7).

Moreover, in NoSolarRad, established stronger latent heating of inner rainbands may also decrease inflow (Fig. 4e) below the primary eyewall and thus reduce upward motion in the eyewall regions after 0000 UTC 16 September (cf. Fig. 5a and Fig. 5c). The differences between CNTL and NoSolarRad in terms of the ice species (cloud ice, snow, graupel) mixing ratio and vertical velocity averaged in the period from 0100 to 0600 UTC 16 September are shown in Fig. 8. The greater eyewall updrafts in the middle to upper levels in CNTL (Figs. 8b,d) favor the production of more ice particles over the moat region (Figs. 8a,c). The broader downdraft area outside the eyewall induced by these ice particles could also help moat formation in CNTL (Figs. 8b,d), as suggested by other studies (e.g., Zhou and Wang 2011; Fang and Zhang 2012).

### *b. Organization of the outer rainbands*

At around 180-km radius, the midlevel (~5 km) ice species mixing ratio is greater in CNTL than in NoSolarRad (Figs. 8a,c). A distinct positive PV anomaly is also evident in the midtroposphere in CNTL (Fig. 10a). All these features can be loosely referred to as features associated with the greater occurrence of

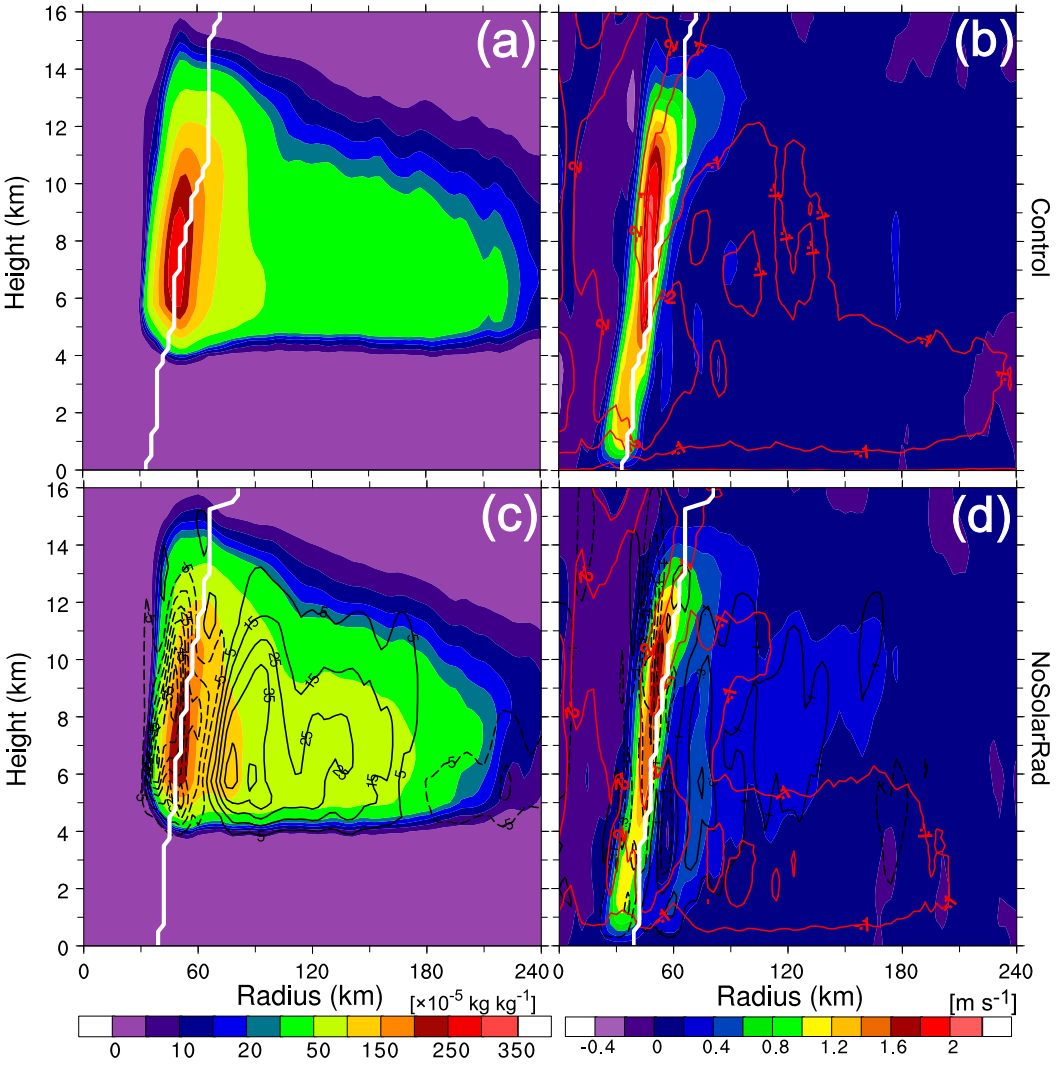


FIG. 8. Vertical cross sections of the 5-h-average azimuth-mean (a) mixing ratio of the sum of cloud ice, snow, and graupel and (b) vertical velocity (shading) and downdrafts (red contours at $-0.1$, $-0.2\,\mathrm{m\,s^{-1}}$) from 0100 to 0600 UTC 16 Sep 2014 for CNTL. (c),(d) As in (a) and (b), respectively, but for NoSolarRad. Black contours are the differences between NoSolarRad and CNTL [solid (dashed) contours denote positive (negative) values; zero is omitted; contour intervals are $10 \times 10^{-5}\,\mathrm{kg\,kg^{-1}}$ and $0.2\,\mathrm{m\,s^{-1}}$ for (c) and (d), respectively]. Superposed white lines denote the RMW.

stratiform cloud in CNTL than in NoSolarRad (e.g., Mapes and Houze 1995). These stratiform clouds located in the northwest quadrants are due mainly to the influence of the northeast VWS (Figs. 2c,d), a mechanism that was suggested by Fang and Zhang (2012).

The evolution of stratiform cloud and the outer rainbands is seen more clearly in vertical cross sections of the wind, equivalent potential temperature $\theta_e$, and PV fields in Figs. 9 and 10. At ~0600 UTC 16 September, the so-called "front-like zone" that separates the warm and moist air of the storm from the relatively dry and cold air in the environment is located right outside the radius of 150 km (Figs. 9a, 11a). A comparison of Figs. 11a and 11b shows that the front-like zone is accompanied by distinct positive horizontal vorticity in the tangential direction ($\eta = \partial\overline{u}/\partial z - \partial\overline{w}/\partial r$, where $\overline{u}$, $\overline{w}$, $z$, and $r$ are the azimuthal means of radial and vertical wind, the height, and the radius). It is suggested that the thermal contrast across the front-like zone is a major contributor to the enhancement of $\eta$ beyond the primary eyewall, and necessary lifting enhances convective activity in the upward branch of the direct thermal circulation with positive $\eta$ (e.g., Fang and Zhang 2012). About 5 h later the inner edge of the front-like zone moved to 120-km radius and the radial gradient of $\theta_e$ across it increased considerably (Fig. 9b). This resulted

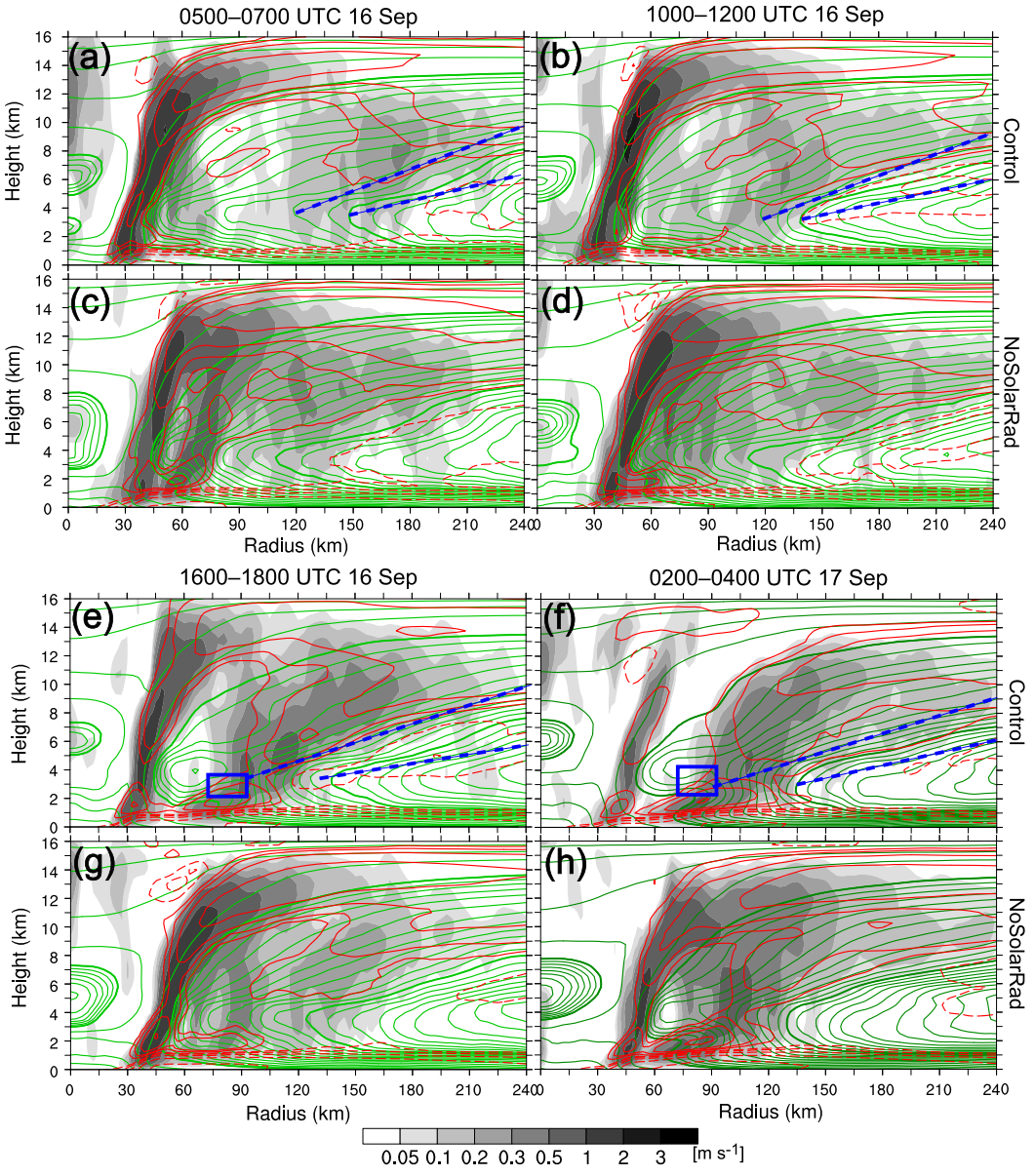


FIG. 9. Vertical cross section of the 2-h azimuthal-mean vertical velocity (shading), equivalent potential temperature $\theta_e$ (green contours), and radial velocity (red contours) for (a),(b),(e),(f) CNTL and (c),(d),(g),(h) NoSolarRad. Thick green solid contours denote 343 (outer radii) and 355 K (inner radii). The $\theta_e$ contour intervals are 1 and 5 K for values smaller and larger than 355 K, respectively. Radial velocity contours are at $\pm1$, $\pm2$, $\pm4$, $\pm8$, and $\pm16\,\mathrm{m\,s^{-1}}$, with dashed lines for negative values. The double dashed blue lines highlight the approximate inner and outer edges of the front-like zone, and the blue box is the related area with enhanced convective instability.

mainly from diabatic heating from active convection on the inner edge of the front-like zone, which increased the $\theta_e$ on the inner edge of the front-like zone, as suggested by Fang and Zhang (2012). Active convection at the inner edge of the front-like zone is also accompanied by low-level convergence (Figs. 12g,i,k), which helps to build a shallow outflow layer directly above the inflow layer between 60- and 105-km radius at ~1100 UTC 16 September (Figs. 4c, 9b). By facilitating the outward advection of the low-level high-$\theta_e$ air from the eyewall region, active convection in the front-like zone not only strengthens the radial gradient of $\theta_e$, but also increases the convective instability in the lower troposphere (Figs. 9e,f). This positive feedback process may result in the inward movement of the front-like zone and the organization of outer rainbands

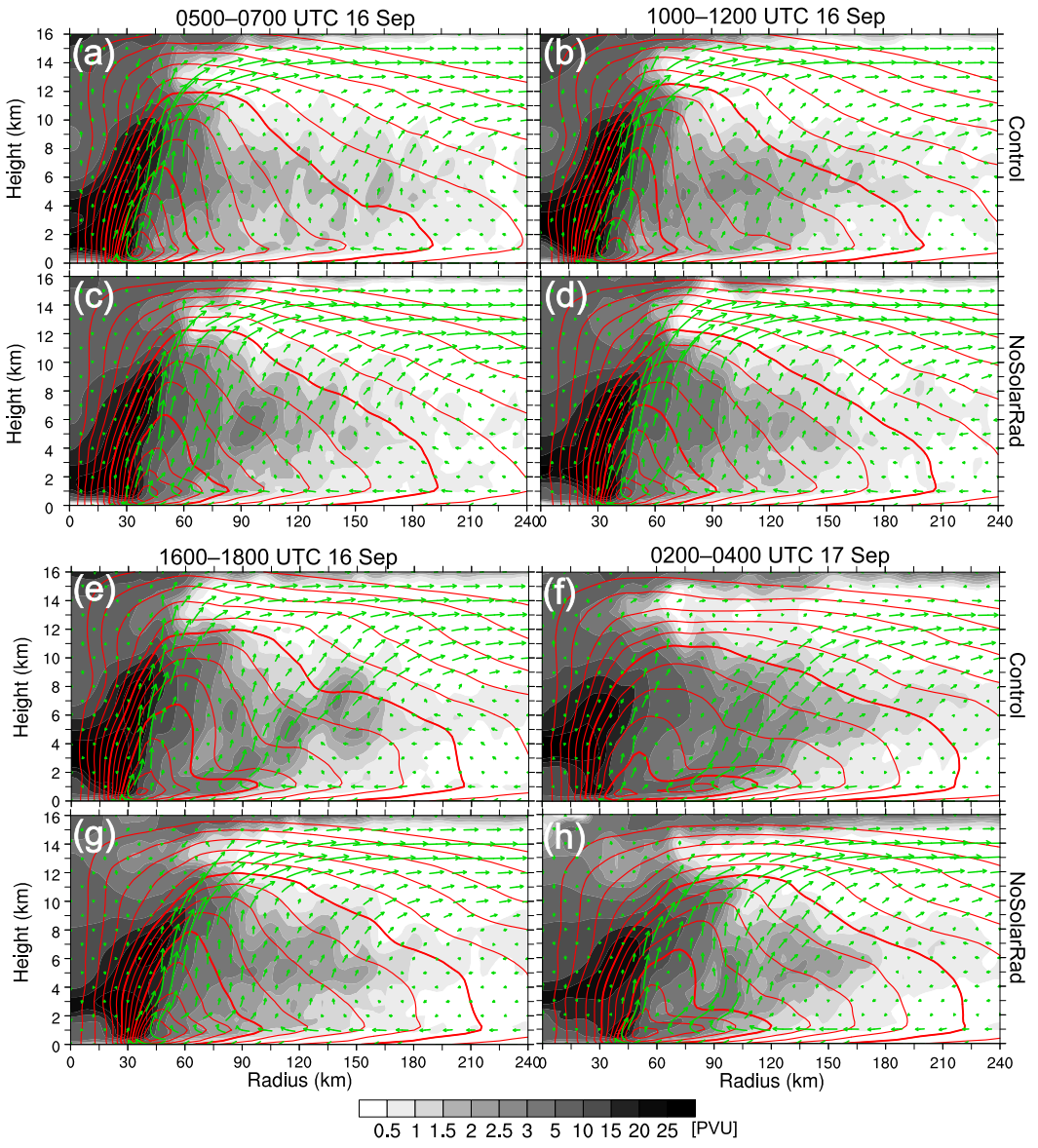


FIG. 10. As in Fig. 9, but for potential vorticity (shaded), tangential velocity (red contours; interval 5 m s$^{-1}$), and secondary circulation vectors. Values of 30 (outer radii) and 50 m s$^{-1}$ (inner radii) are shown by thick red contours.

(Figs. 2i, 5a, 5b, 9e, 9f). The organization of outer rainbands finally leads to the formation of the secondary convective ring/eyewall at 75–90-km radius at ~1700 UTC 16 September (Figs. 9e,f). Meanwhile, the tangential wind strengthened considerably in the outer-core area and finally formed a secondary maximum in the SEF region, accompanying a clearly separate PV column (Figs. 10a,b,e,f).

In contrast, the inner rainbands developed vigorously with strong updrafts between ~60- and 90-km radius in NoSolarRad (Figs. 9c,d,g,h) as a result of increased net radiative cooling at levels from 8 to 15 km (Fig. 6c). Finally, convection in the outer-core region (150–210 km) is not as well organized as that in CNTL in forming strong outer rainbands (Figs. 9c,d,g,h, 10c,d,g,h), because of the compensating downdrafts of the inner rainbands and a shorter filamentation time in the outer-core region, which is explained further in the next paragraph (Fig. 13b). In NoSolarRad, strong heating of the inner rainbands results in increased (reduced) low-level tangential wind outside (near and inside) the RMW (Shapiro and Willoughby 1982), so the expansion of the tangential wind was continuous outside the eyewall without a gap between the eyewall and the outer region. Therefore, a stronger WISHE process than in CNTL in the corresponding moat region prevented moat formation (Figs. 10g,e).

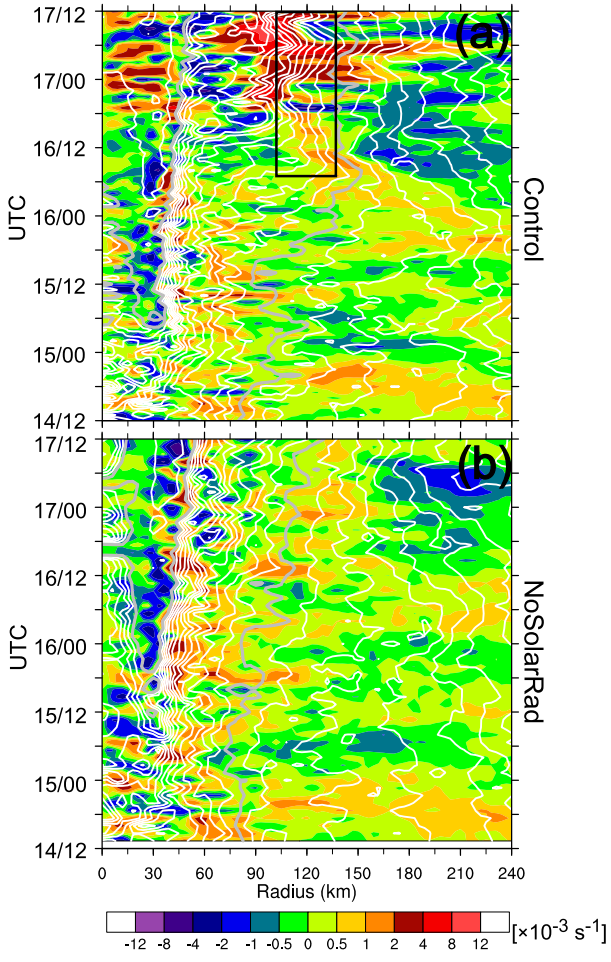


FIG. 11. Hovmöller plots of the horizontal vorticity (shading) and equivalent potential temperature $\theta_e$ (white contours) at a height of 3.5 km for (a) CNTL and (b) NoSolarRad. The interval of $\theta_e$ is as in Fig. 9 with values of 343 (outer radii) and 355 K (inner radii) shown by solid gray contours. The black box indicates the approximate position of the front-like zone.

Figure 13a presents the radial distribution of PV after the formation of the stratiform region at 150–210-km radius averaged between 0500 and 0700 UTC 16 September in CNTL (Figs. 2d, 3c). This clearly shows greater PV in CNTL in the stratiform region outside 150-km radial distance than in NoSolarRad, and greater PV in NoSolarRad between 70 and 120 km than in CNTL, related to the inner rainbands. The distinct midlevel PV anomaly means that the tangential wind and its radial gradient on the inner side of the midlevel PV maximum were weaker in CNTL than in NoSolarRad (Figs. 10a,c). Correspondingly, the filamentation time scale {defined as $[-(\overline{v}/r)(\partial\overline{v}/\partial r)]^{-0.5}$ by Rozoff et al. (2006), with $\overline{v}$ denoting the azimuthal-mean tangential velocity} at 120–180-km radius was much longer in CNTL than in NoSolarRad (Fig. 13b), which is therefore a more convection-friendly region because of the relatively weak straining process there (Rozoff et al. 2006). On the other hand, the radial gradient of the tangential wind on the outer side of RMW was larger in CNTL, which favored the formation of a rapid filamentation zone that suppressed convection and eventually resulted in moat formation near the radius (~65–80 km) at which the filamentation time scale reached its minimum (~30 min; Fig. 13b).

### c. *Boundary layer responses*

The importance of hurricane BL dynamics for understanding SEF is widely acknowledged, although different views exist on its role (Huang et al. 2012; Abarca and Montgomery 2013; Kepert 2013; Kepert and Nolan 2014; Zhang et al. 2017). In this subsection, we will show how the BL responses to different forcing from above contribute differently before and during SEF in CNTL compared with NoSolarRad. Before rapid intensification had finished, the BL convergence was concentrated mainly below the eyewall region and the maximum tangential wind tendency was located inside the RMW (Fig. 12a). However, there was a separate convergence center associated with rainbands located at 60–90-km radius in NoSolarRad, above which the tangential tendency at the top of the BL was greater than that in CNTL (Figs. 12a–d). With the start of outer-rainband organization in CNTL, another BL convergence center began to form outside the 90-km radius while the tangential wind tendency decreased inside the RMW (Fig. 12e). Along with the further development of outer rainbands, the outer convergence center moved inward and strengthened, while the accompanying tangential wind tendency increased and moved gradually inward. In the meantime, the tangential wind in the moat region increased little, while the tangential wind under the primary eyewall began to decrease after ~1200 UTC 16 September (Figs. 12g,i,k). Contrary to the CNTL, the tangential wind increased more outside of the RMW in NoSolarRad because of the greater convective heating of the inner rainbands, especially in the moat region (Figs. 12f,h,j,l). Generally weaker convergence near the RMW above the BL in NoSolarRad was also consistent with a relatively weak eyewall updraft (Figs. 5, 12).

Once the outer rainbands in the CNTL were well organized, the tangential wind increased significantly at the outer side of the rainbands with strong convergence and slightly decreased on the inner side with strong divergence (Fig. 12k), which was likely the response to outer rainband heating and BL friction (Fang and Zhang 2012; Rozoff et al. 2012; Sun et al. 2013) and was crucial to subsequent SEF. Meanwhile, the tangential wind near

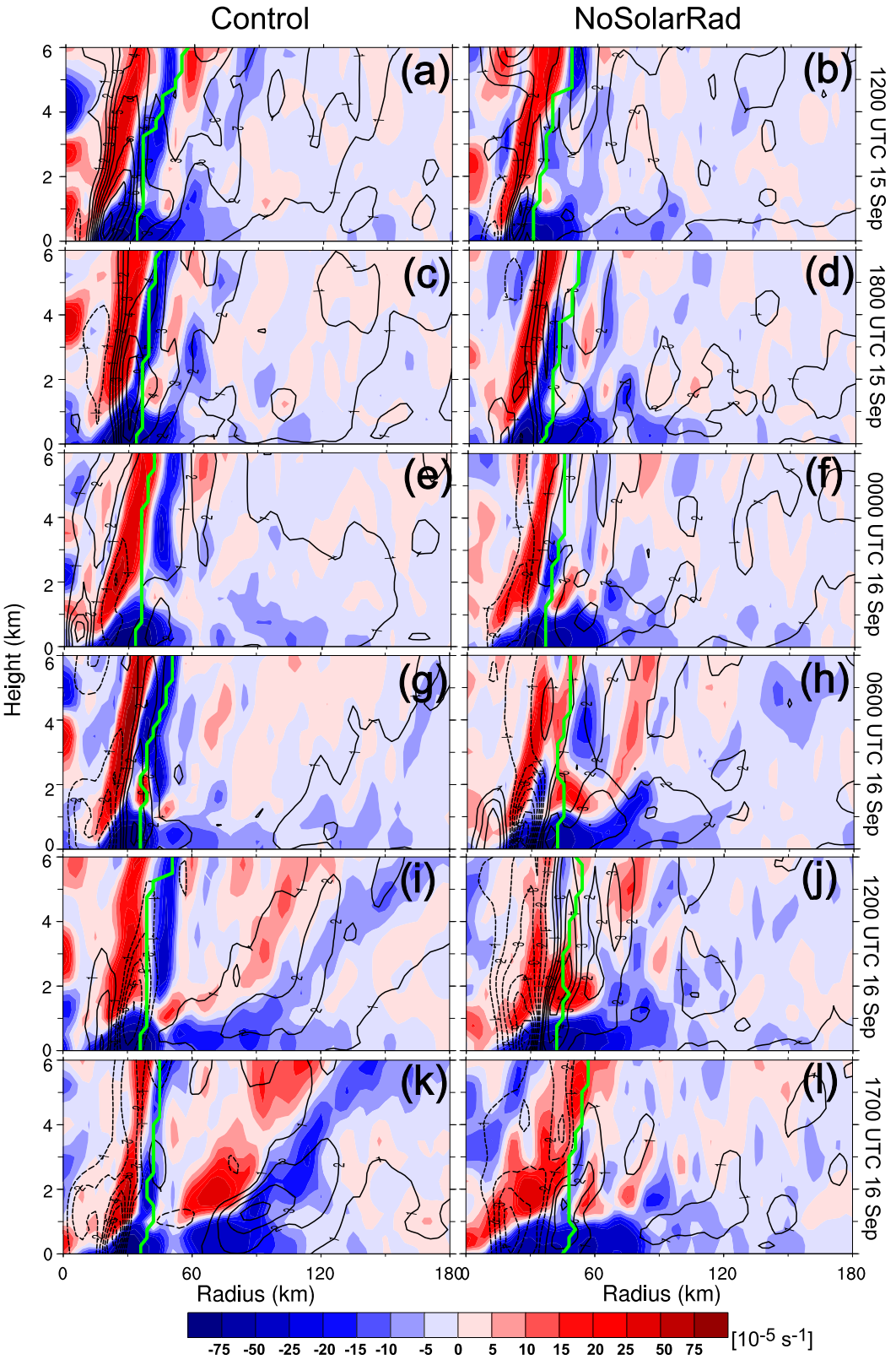


FIG. 12. Radius–height plot of azimuthally and temporally averaged divergence (shading) and 3-hourly tangential velocity change [contours; interval 1 m $s^{-1}$; solid (dashed) lines denote positive (negative) values; zero is omitted] averaged over ($t - 1$ h, $t + 1$ h). Superposed green lines denote the RMW.

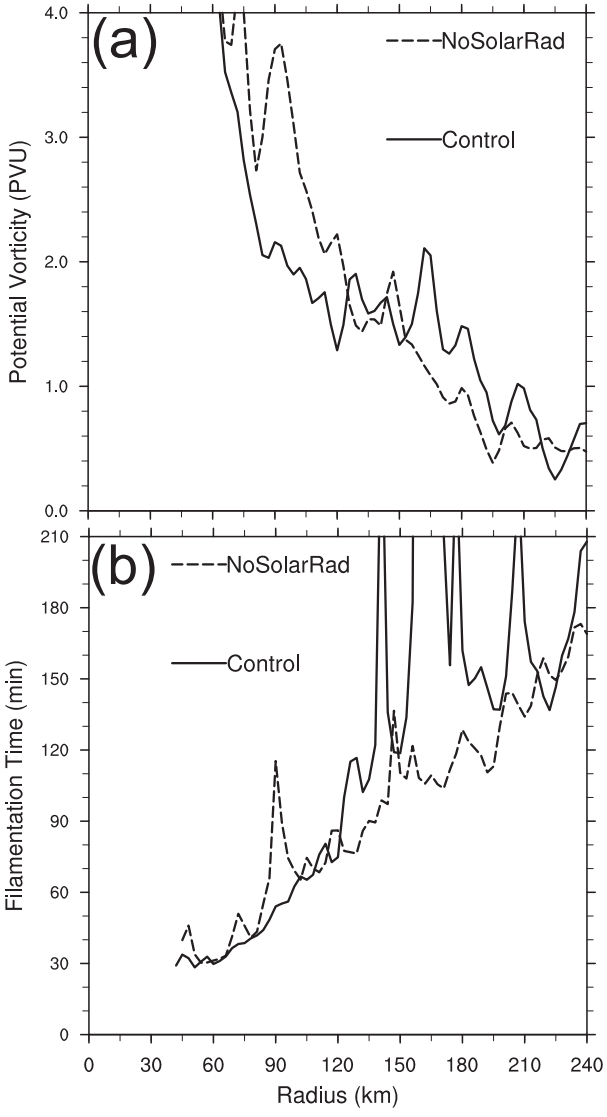


FIG. 13. Azimuthal-mean (a) potential vorticity and (b) filamentation time at a height of 5 km averaged from 0500 to 0700 UTC 16 Sep 2014.

RMW and of the moat ceased to increase. At this time in CNTL, there were two separate maximum convergence centers in the BL, and the moat formed between them. The strong convergence center peaking at a radius of 60–90 km and rooted in the BL was largely tied to the enhanced updrafts in the outer rainbands (Figs. 5a, 5b, 9e, 12k). These results are also consistent with recent findings (Wang et al. 2016) that the broadening of tangential wind above the BL results primarily from inward angular momentum transport by the mid- to lower-tropospheric inflow induced by both convective and stratiform heating in spiral rainbands (Figs. 9a,b,e, 10a,b,e). Some recent studies have argued that the unbalanced response of radial inflow convergence within and just above the BL to the expanding tangential wind is a potentially important mechanism for initiating and sustaining deep convection in a concentrated zone in the hurricane outer-core region, and thus for the SEF (Huang et al. 2012; Abarca and Montgomery 2013).

In contrast, there is only one continuous convergence zone in the BL below the eyewall in the NoSolarRad, without a separated strong convergence center in the outer core as seen in CNTL because of the stronger inner rainbands in the NoSolarRad (Figs. 12l, 2m, 3k). As a result, the tangential wind continued to increase near the RMW in NoSolarRad, which prevented the formation of two separated tangential wind maxima or a moat and eventual SEF.

### *d. Balanced aspects of SEF*

To address quasi-balanced aspects of SEF, we employ the Sawyer–Eliassen (S–E) equation (see appendix) to study the symmetric response of a balanced vortex with different structures to different fixed latent heating resulting from different radiation effects. The diagnosed secondary circulation and tangential wind tendency from the S–E model will illustrate which of vortex structure or latent heating forcing is more important for moat formation and SEF in the early and later stages of SEF. The S–E model has been shown to be a valid tool and is widely used to understand the evolution of mean swirling circulation in idealized axisymmetric vortices (e.g., Shapiro and Willoughby 1982; Hack and Schubert 1986; Hendricks et al. 2004; Bui et al. 2009; Pendergrass and Willoughby 2009; Sun et al. 2013). Our focus is the response of the vortex to latent heating forcing, so only latent heating rate is retained as a forcing term. The coefficients and forcing terms of the S–E equation related to the background vortex and latent heating are calculated from the WRF output.

In previous sections, it was shown that a small partial moat (extending only partway round the storm) occurred in CNTL at ~0600 UTC 16 September (Figs. 2d, 3c, 5a, 9a, 12g) in the early stages of SEF, whereas stronger inner rainbands strengthened at the corresponding radii in NoSolarRad (Figs. 2h, 3f, 5c, 9c, 12h). The 2-h azimuthal-mean vortex structures of inertial stability and latent heating forcing are shown for CNTL and NoSolarRad over the period from 0500 to 0700 UTC 16 September (Figs. 14a,d), when the S–E equation is applied. The features of transverse circulation were captured reasonably well by the balanced response diagnosed from the S–E equation, especially above the BL (cf. Figs. 9a and 14b, and Figs. 9c and 14e). The S–E-derived circulation is different from the WRF simulation in the BL because the BL friction forcing term is not included in the present S–E equation calculation. There

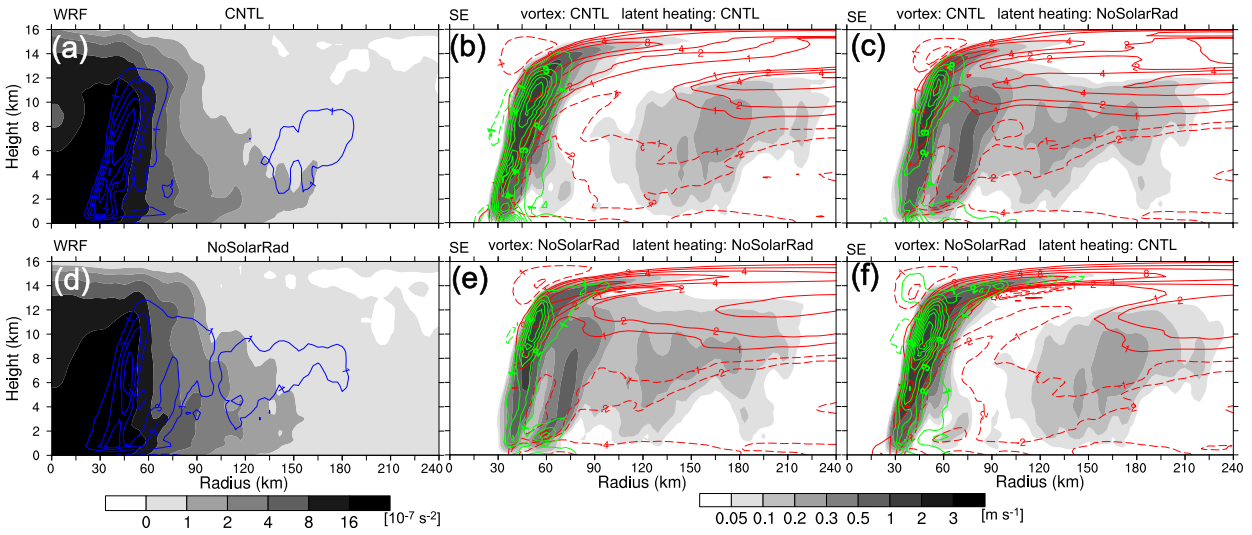


FIG. 14. Radius–height cross sections of the 2-h azimuthal mean of the inertial stability parameter $I^2$ (shading) and latent heating (blue contours; $10^{-3}$ K s$^{-1}$) from WRF output in (a) CNTL and (d) NoSolarRad, and of vertical velocity (shading), radial velocity (red contours; m s$^{-1}$), and the combined contribution of radial advection of absolute vorticity and vertical advection of tangential wind to the tangential wind tendency (green contours; $10^{-3}$ m s$^{-2}$) from S–E model calculations using (b) the background vortex structure and diabatic heating from CNTL, (c) the background vortex structure of CNTL and diabatic heating from NoSolarRad, (e) the background vortex structure and diabatic heating from NoSolarRad, and (f) the background vortex structure of NoSolarRad and diabatic heating from CNTL. The period is from 0500 to 0700 UTC 16 Sep 2014.

are downdrafts in the moat region of CNTL where there is little latent heating. The prognostic equation for the azimuthal-mean tangential wind can be written as follows (Xu and Wang 2010):

$$\frac{\partial \overline{v}}{\partial t} = -\overline{u}(f + \overline{\zeta}) - \overline{w}\frac{\partial \overline{v}}{\partial z} + \overline{F} \quad \text{and} \tag{1}$$

$$\overline{F} = -\overline{u'\zeta'} - \overline{w'\frac{\partial v'}{\partial z}} + \overline{F_{sg}}, \tag{2}$$

where $z$ is height; $f$ is the Coriolis parameter; and $\overline{v}$, $\overline{u}$, $\overline{w}$, and $\overline{\zeta}$ are azimuthally averaged tangential and radial velocity, vertical velocity, and relative vorticity, respectively. The first two terms of $\overline{F}$ represent the azimuthal-mean eddy radial and vertical fluxes of the asymmetric tangential wind, respectively, and $\overline{F_{sg}}$ is the term coming from subgrid-scale processes in the numerical model, comprising both diffusive and surface layer processes. The combined contribution of the radial advection of absolute vorticity and the vertical advection of tangential wind to the tangential wind tendency $\dot{v}$ is calculated using the diagnosed radial and vertical velocities from the S–E equation. The frictional force and eddy contribution are ignored here. The value of $\dot{v}$ is much smaller in the low-level moat region in CNTL than in NoSolarRad (cf. Figs. 14b and 14e), which favors the relatively weak tangential wind in the moat region of CNTL. The S–E-diagnosed results qualitatively capture the positive tendencies but reproduce the negative tendencies inside the RMW less well than the WRF-simulated results (Figs. 12g,h). The smaller contribution in CNTL above 1 km is due predominantly to weaker vertical transport of momentum.

Some additional idealized experiments are also conducted with the S–E model to more thoroughly investigate the relative importance of latent heating forcing and vortex structure on moat formation and SEF. Figure 14c shows the results with the vortex structure of CNTL but the latent heating of NoSolarRad, while Fig. 14f has the vortex structure of NoSolarRad but the latent heating forcing of CNTL. A similar transverse circulation to that in Fig. 14e and greater $\dot{v}$ at the BL top of the moat region also occurs in Fig. 14c, while the transverse circulation pattern and tangential wind tendency in Fig. 14f are similar to those in Fig. 14b. Consequently, it is inferred that in the early stages of SEF the absence of diabatic heating forcing and the resulting smaller $\dot{v}$ in the moat region in CNTL are more important than the role of background vortex wind structure for moat formation and the later smaller negative shear vorticity due to horizontal shear of tangential wind at the outer edge of the moat region (Fig. 10e).

After 0600 UTC 16 September, tangential wind clearly expanded outward, especially near the 90-km radius (Fig. 4a) and so the inertial stability [see Eq. (A4)]

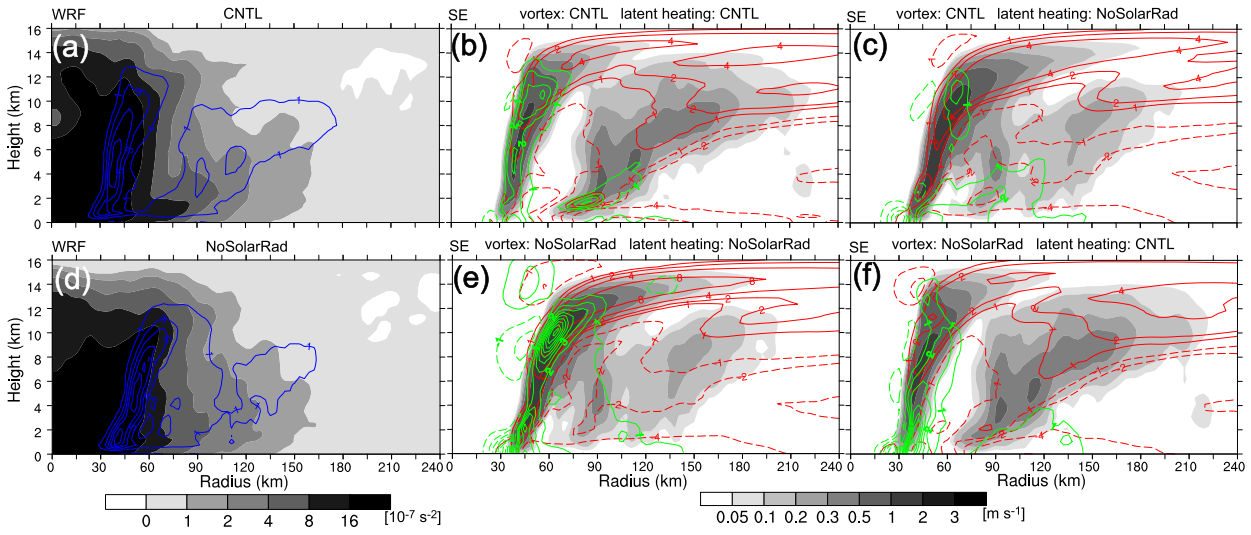


FIG. 15. As in Fig. 14, but for the period from 1600 to 1800 UTC 16 Sep 2014.

also increased in this region (Fig. 15a). Meanwhile, latent heating was enhanced more by the strengthening of outer rainbands there in CNTL than in NoSolarRad (cf. Figs. 15a and 15d). The kinetic efficiency by which latent heating can be retained as local kinetic energy will also increase where the tangential wind expands, as suggested by Rozoff et al. (2012). The relative importance of latent heating and vortex structure on the spinup of an outer eyewall is investigated in the late stage closer to SEF, using a similar method to that employed in the early stage of SEF with the S–E model. With the combined effects of stronger latent heating and inertial stability in the outer rainbands in CNTL, $\dot{v}$ there is greater than in NoSolarRad (cf. Figs. 15b and 15e), and it is also greater than that in the other two diagnosed solutions from the S–E equation, one with the vortex structure of CNTL but the latent heating of NoSolarRad (Fig. 15c), the other with the vortex structure of NoSolarRad but the latent heating of CNTL (Fig. 15f). Neither Fig. 15c nor Fig. 15f captures the concentrated region of large positive tendencies in the SEF region shown in Fig. 15b. Therefore, the enhanced stability and latent heating contribute comparably to the positive wind tendencies in the SEF region during the later stage of SEF. This interpretation is consistent with Rozoff et al. (2012), although the frictional forcing is not considered here.

## 5. Concluding remarks

This work examines the sensitivity of hurricane SEF to solar insolation through high-resolution convection-permitting full-physics simulations of Hurricane Edouard (2014) using the WRF Model. In a sensitivity experiment, the solar shortwave radiation is shut off about 2 days prior to SEF in the control run. Comparison of the two runs shows that the hurricane SEF may be highly sensitive to the diurnal solar insolation cycle.

During the first day of the storm intensification period, the shortwave solar insolation in the CNTL heats the mid- to upper-level troposphere, including the moat region in the daytime, leading to a net stabilization effect and suppressing the development of convection, which is consistent with previous findings (Melhauser and Zhang 2014; TZ16). As the storm develops there is a weakened WISHE feedback process involving moist convection, convergence of radial inflow, tangential wind acceleration, and the surface heat and energy fluxes in the moat region. Lack of latent heating in the moat region also enhances the subsidence there, as also suggested by Rozoff et al. (2012).

Meanwhile, in the outer-core region of the storm, there are outer rainbands favored by the VWS. The warm temperature advection induced by subsidence in the moat region and evaporative cooling of the stratiform precipitation of the outer rainbands collude to sharpen the radial gradient of low-level equivalent potential temperature into a front-like zone, resulting in active convective bursts on its inner edge (Fang and Zhang 2012). The filamentation time was also much longer just inside and outside of the SEF region shortly before the storm reached its peak intensity in CNTL. A positive feedback between the front-like zone and leading convection on its inner edge results in the development of outer rainbands and eventually a typical SEF with a clear moat region in

CNTL. In the sensitivity experiment without solar radiation, in contrast, overly active inner rainbands occur persistently between the eyewall and outer rainbands, so there is no space for moat formation and no subsequent SEF.

In brief, the solar insolation impacts the SEF through influencing the interaction of the primary eyewall, inner rainbands, and outer rainbands via the radiation–thermodynamics–convection pathway. Diagnosis using the Sawyer–Eliassen equation and sensitivity experiments, in which vortex structure and latent heating forcing are switched, further validates the absence of diabatic heating in the moat region as a more important factor to smaller tangential wind tendency in the moat region. This diagnosis also emphasizes the benefit to moat formation during the early stage of SEF in an environment that favors rich convection. While these results are derived from applying an axisymmetric balanced Sawyer–Eliassen model to WRF output with only latent heating forcing, the importance of both inertial stability and latent heating forcing in the SEF process are expected to be relevant accounting for nonlinear BL dynamics in SEF (Huang et al. 2012).

The storm BL responses to latent heating from the eyewall and rainband, represented by the convergence, are also quite different between CNTL with a real diurnal radiation cycle and NoSolarRad without solar insolation. In NoSolarRad, there is only one strong convergence region induced by active inner rainbands and the primary eyewall, while there is a second BL convergence center in the outer core in the CNTL. As a result, no secondary maximum of the tangential winds occurs in the BL in the NoSolarRad.

Although the sensitivity of SEF to solar insolation is clearly shown in this case study of Hurricane Edouard (2014), the impacts of the diurnal radiation cycle on the timing and radial location of SEF, and the interplay between double eyewalls during ERC, need to be investigated further using observations and simulations, for which results will be presented in due course. The robustness of the sensitivity of SEF to diurnal solar insolation cycles might be further examined for tropical cyclones with different intensities and sizes.

*Acknowledgments.* The authors thank Yonghui Weng for performing the real-time ensemble data assimilation and Erin B. Munsell for performing the control run and sensitivity experiments. We also benefited from discussions with Da-Lin Zhang, Yuqing Wang, Chun-Chieh Wu, and Ping Zhu. The authors acknowledge the helpful comments of three anonymous reviewers. This work was supported by the National Nature Science Foundation of China (Grants 41675054 and 41461164008). Computing at the Texas Advanced Computing Center (TACC) and NOAA Jet clusters at the Earth System Research Laboratory (ESRL) is acknowledged.

## APPENDIX

### Sawyer–Eliassen Equation

Under the constraints of hydrostatic and gradient wind balance, the Sawyer–Eliassen equation in radius–pseudoheight coordinates for the transverse circulation induced by axisymmetric latent heating and friction can be written as follows (Montgomery et al. 2006; Fudeyasu and Wang 2011):

$$\frac{\partial}{\partial r}\left(\frac{A}{r}\frac{\partial\overline{\psi}}{\partial r}+\frac{B}{r}\frac{\partial\overline{\psi}}{\partial z}\right)+\frac{\partial}{\partial z}\left(\frac{C}{r}\frac{\partial\overline{\psi}}{\partial z}+\frac{B}{r}\frac{\partial\overline{\psi}}{\partial r}\right)=\frac{\partial\overline{Q}}{\partial r}-\frac{\partial\overline{\xi F}}{\partial z}, \tag{A1}$$

where the toroidal streamfunction $\overline{\psi}$ is related to the azimuthal-mean radial velocity $\overline{u}$ and vertical velocity $\overline{w}$ for a Boussinesq fluid by $\overline{u}=-(1/r)(\partial\overline{\psi}/\partial z)$ and $\overline{w}=(1/r)(\partial\overline{\psi}/\partial r)$. The three parameters on the left-hand side of Eq. (A1) related to the thermodynamic and dynamic features of the background vortex are defined as

$$A=\overline{N^2}=\frac{g}{\theta_0}\frac{\partial\overline{\theta}}{\partial z}, \tag{A2}$$

$$B=-\overline{\xi}\frac{\partial\overline{v}}{\partial z}, \quad \text{and} \tag{A3}$$

$$C=\overline{I^2}=\overline{\xi}\,\overline{\eta}, \quad \text{(i.e., inertial stability)}, \tag{A4}$$

where $\overline{v}$, $\overline{\theta}$, and $\overline{\eta}$ are the azimuthal means of tangential wind, potential temperature, and absolute vertical vorticity, respectively, and $\overline{\xi}=f_0+2\overline{v}/r$ is the vortex inertial parameter of the swirling flow. The forcing due to heating on the right-hand side of Eq. (A1) is defined as

$$\overline{Q}=\frac{g}{\theta_0}\left(-\overline{u'\frac{\partial\theta'}{\partial r}}-\overline{w'\frac{\partial\theta'}{\partial z}}+\overline{\dot{\theta}}\right), \tag{A5}$$

where the first two terms represent the azimuthal-mean eddy radial and vertical fluxes of the asymmetric potential temperature and $\overline{\dot{\theta}}$ is the azimuthal-mean diabatic heating rate. The momentum forcing $\overline{F}$ is defined similarly to Eq. (2) in section 4d of the main text. The reader is referred to Fudeyasu and Wang (2011) or Montgomery et al. (2006) for the meanings of other symbols and for details of the calculation.

## REFERENCES


Abarca, S. F., and K. L. Corbosiero, 2011: Secondary eyewall formation in WRF simulations of Hurricanes Rita and Katrina (2005). *Geophys. Res. Lett.*, **38**, L07802, doi:10.1029/2011GL047015.

——, and M. T. Montgomery, 2013: Essential dynamics of secondary eyewall formation. *J. Atmos. Sci.*, **70**, 3216–3230, doi:10.1175/JAS-D-12-0318.1.

——, ——, S. A. Braun, and J. P. Dunion, 2016: On the secondary eyewall formation of Hurricane Edouard (2014). *Mon. Wea. Rev.*, **144**, 3321–3331, doi:10.1175/MWR-D-15-0421.1.

Braun, S., P. Newman, and G. Heymsfield, 2016: NASA's Hurricane and Severe Storm Sentinel (HS3) investigation. *Bull. Amer. Meteor. Soc.*, **97**, 2085–2102, doi:10.1175/BAMS-D-15-00186.1.

Bui, H. H., R. K. Smith, M. T. Montgomery, and J. Peng, 2009: Balanced and unbalanced aspect of tropical cyclone intensification. *Quart. J. Roy. Meteor. Soc.*, **135**, 1715–1731, doi:10.1002/qj.502.

Dudhia, J., 1989: Numerical study of convection observed during the Winter Monsoon Experiment using a mesoscale two-dimensional model. *J. Atmos. Sci.*, **46**, 3077–3107, doi:10.1175/1520-0469(1989)046<3077:NSOCOD>2.0.CO;2.

Emanuel, K. A., 1986: An air–sea interaction theory for tropical cyclones. Part I: Steady-state maintenance. *J. Atmos. Sci.*, **43**, 585–605, doi:10.1175/1520-0469(1986)043<0585:AASITF>2.0.CO;2.

Fang, J., and F. Zhang, 2012: Effect of beta shear on simulated tropical cyclones. *Mon. Wea. Rev.*, **140**, 3327–3346, doi:10.1175/MWR-D-10-05021.1.

Fudeyasu, H., and Y. Wang, 2011: Balanced contribution to the intensification of a tropical cyclone simulated in TCM4: Outer-core spinup process. *J. Atmos. Sci.*, **68**, 430–449, doi:10.1175/2010JAS3523.1.

Grell, G. A., and S. R. Freitas, 2014: A scale and aerosol aware stochastic convective parameterization for weather and air quality modeling. *Atmos. Chem. Phys.*, **14**, 5233–5250, doi:10.5194/acp-14-5233-2014.

Hack, J. J., and W. H. Schubert, 1986: Nonlinear response of atmospheric vortices to heating by organized cumulus convection. *J. Atmos. Sci.*, **43**, 1559–1573, doi:10.1175/1520-0469(1986)043<1559:NROAVT>2.0.CO;2.

Hence, D. A., and R. A. Houze Jr., 2012: Vertical structure of tropical cyclones with concentric eyewalls as seen by the TRMM Precipitation Radar. *J. Atmos. Sci.*, **69**, 1021–1036, doi:10.1175/JAS-D-11-0119.1.

Hendricks, E. A., M. T. Montgomery, and C. A. Davis, 2004: The role of "vortical" hot towers in the formation of tropical cyclone Diana (1984). *J. Atmos. Sci.*, **61**, 1209–1232, doi:10.1175/1520-0469(2004)061<1209:TROVHT>2.0.CO;2.

Hong, S., and J. J. Lim, 2006: The WRF single-moment 6-class microphysics scheme (WSM6). *J. Korean Meteor. Soc.*, **42**, 129–151.

——, Y. Noh, and J. B. Dudhia, 2006: A new vertical diffusion package with an explicit treatment of entrainment processes. *Mon. Wea. Rev.*, **134**, 2318–2341, doi:10.1175/MWR3199.1.

Houze, R. A., S.-S. Chen, B. F. Smull, W.-C. Lee, and M. M. Bell, 2007: Hurricane intensity and eyewall replacement. *Science*, **315**, 1235–1239, doi:10.1126/science.1135650.

Huang, Y.-H., M. T. Montgomery, and C.-C. Wu, 2012: Concentric eyewall formation in Typhoon Sinlaku (2008). Part II: Axisymmetric dynamical processes. *J. Atmos. Sci.*, **69**, 662–674, doi:10.1175/JAS-D-11-0114.1.

Judt, F., and S. S. Chen, 2010: Convectively generated vorticity in rainbands and formation of the secondary eyewall in Hurricane Rita of 2005. *J. Atmos. Sci.*, **67**, 3581–3599, doi:10.1175/2010JAS3471.1.

Kepert, J. D., 2013: How does the boundary layer contribute to eyewall replacement cycles in axisymmetric tropical cyclones? *J. Atmos. Sci.*, **70**, 2808–2830, doi:10.1175/JAS-D-13-046.1.

——, and D. S. Nolan, 2014: Reply to "Comments on 'How does the boundary layer contribute to eyewall replacement cycles in axisymmetric tropical cyclones?'." *J. Atmos. Sci.*, **71**, 4692–4704, doi:10.1175/JAS-D-14-0014.1.

Kossin, J. P., and M. Sitkowski, 2009: An objective model for identifying secondary eyewall formation in hurricanes. *Mon. Wea. Rev.*, **137**, 876–892, doi:10.1175/2008MWR2701.1.

Kuo, H.-C., L. Y. Lin, C. P. Chang, and R. T. Williams, 2004: The formation of concentric vorticity structures in typhoons. *J. Atmos. Sci.*, **61**, 2722–2734, doi:10.1175/JAS3286.1.

——, W. H. Schubert, C.-L. Tsai, and Y.-F. Kuo, 2008: Vortex interaction and barotropic aspects of concentric eyewall formation. *Mon. Wea. Rev.*, **136**, 5183–5198, doi:10.1175/2008MWR2378.1.

——, C.-P. Chang, Y.-T. Yang, and H.-J. Jiang, 2009: Western North Pacific typhoons with concentric eyewalls. *Mon. Wea. Rev.*, **137**, 3758–3770, doi:10.1175/2009MWR2850.1.

Li, Q., and Y. Wang, 2012: Formation and quasi-periodic behavior of outer spiral rainbands in a numerically simulated tropical cyclone. *J. Atmos. Sci.*, **69**, 997–1020, doi:10.1175/2011JAS3690.1.

Maclay, K. S., M. DeMaria, and T. H. Vonder Haar, 2008: Tropical cyclone inner core kinetic energy evolution. *Mon. Wea. Rev.*, **136**, 4882–4898, doi:10.1175/2008MWR2268.1.

Mapes, B. E., and R. A. Houze Jr., 1995: Diabatic divergence profiles in western Pacific mesoscale convective systems. *J. Atmos. Sci.*, **52**, 1807–1828, doi:10.1175/1520-0469(1995)052<1807:DDPIWP>2.0.CO;2.

Melhauser, C., and F. Zhang, 2014: Diurnal radiation cycle impact on the pregenesis environment of Hurricane Karl (2010). *J. Atmos. Sci.*, **71**, 1241–1259, doi:10.1175/JAS-D-13-0116.1.

Menelaou, K., M. K. Yau, and Y. Martinez, 2012: On the dynamics of the secondary eyewall genesis in Hurricane Wilma (2005). *Geophys. Res. Lett.*, **39**, L04801, doi:10.1029/2011GL050699.

Mlawer, E. J., S. J. Taubman, P. D. Brown, M. J. Iacono, and S. A. Clough, 1997: Radiative transfer for inhomogeneous atmosphere: RRTM, a validated correlated-k model for the longwave. *J. Geophys. Res.*, **102**, 16 663–16 682, doi:10.1029/97JD00237.

Montgomery, M. T., and R. J. Kallenbach, 1997: A theory for vortex Rossby-waves and its application to spiral bands and intensity changes inhurricanes. *Quart. J. Roy. Meteor. Soc.*, **123**, 435–465, doi:10.1002/qj.49712353810.

——, M. E. Nicholls, T. A. Cram, and A. B. Saunders, 2006: A vortical hot tower route to tropical cyclogenesis. *J. Atmos. Sci.*, **63**, 355–386, doi:10.1175/JAS3604.1.

Moon, Y., and D. S. Nolan, 2010: The dynamic response of the hurricane wind field to spiral rainband heating. *J. Atmos. Sci.*, **67**, 1779–1805, doi:10.1175/2010JAS3171.1.

Munsell, E. B., F. Zhang, J. A. Sippel, S. A. Braun, and Y. Weng, 2017: Dynamics and predictability of the intensification of Hurricane Edouard (2014). *J. Atmos. Sci.*, **74**, 573–595, doi:10.1175/JAS-D-16-0018.1.

Pendergrass, A. G., and H. E. Willoughby, 2009: Diabatically induced secondary flows in tropical cyclones. Part I: Quasisteady

forcing. *Mon. Wea. Rev.*, **137**, 805–821, doi:10.1175/2008MWR2657.1.

Qiu, X., and Z.-M. Tan, 2013: The roles of asymmetric inflow forcing induced by outer rainbands in tropical cyclone secondary eyewall formation. *J. Atmos. Sci.*, **70**, 953–974, doi:10.1175/JAS-D-12-084.1.

——, ——, and Q. Xiao, 2010: The roles of vortex Rossby waves in hurricane secondary eyewall formation. *Mon. Wea. Rev.*, **138**, 2092–2109, doi:10.1175/2010MWR3161.1.

Rogers, R. F., and Coauthors, 2013: NOAA's Hurricane Intensity Forecasting Experiment (IFEX): A progress report. *Bull. Amer. Meteor. Soc.*, **94**, 859–882, doi:10.1175/BAMS-D-12-00089.1.

Rozoff, C. M., W. H. Schubert, B. D. McNoldy, and J. P. Kossin, 2006: Rapid filamentation zones in intense tropical cyclones. *J. Atmos. Sci.*, **63**, 325–340, doi:10.1175/JAS3595.1.

——, D. S. Nolan, J. P. Kossin, F. Zhang, and J. Fang, 2012: The roles of an expanding wind field and inertial stability in tropical cyclone secondary eyewall formation. *J. Atmos. Sci.*, **69**, 2621–2643, doi:10.1175/JAS-D-11-0326.1.

Shapiro, L. J., and H. E. Willoughby, 1982: The response of balanced hurricanes to local sources of heat and momentum. *J. Atmos. Sci.*, **39**, 378–394, doi:10.1175/1520-0469(1982)039<0378:TROBHT>2.0.CO;2.

Smith, R. K., M. T. Montgomery, and S. V. Nguyen, 2009: Tropical cyclone spinup revisited. *Quart. J. Roy. Meteor. Soc.*, **135**, 1321–1335, doi:10.1002/qj.428.

Stewart, S. R., 2014: Hurricane Edouard (AL062014), 11–19 September 2014. National Hurricane Center Tropical Cyclone Rep., 19 pp. [Available online at http://www.nhc.noaa.gov/data/tcr/AL062014_Edouard.pdf.]

Sun, Y., Y. Jiang, B. Tan, and F. Zhang, 2013: The governing dynamics of the secondary eyewall formation of Typhoon Sinlaku (2008). *J. Atmos. Sci.*, **70**, 3818–3837, doi:10.1175/JAS-D-13-044.1.

Tang, X., and F. Zhang, 2016: Impacts of the diurnal radiation cycle on the formation, intensity and structure of Hurricane Edouard (2014). *J. Atmos. Sci.*, **73**, 2871–2892, doi:10.1175/JAS-D-15-0283.1.

Terwey, W. D., and M. T. Montgomery, 2008: Secondary eyewall formation in two idealized, full-physics modeled hurricanes. *J. Geophys. Res.*, **113**, D12112, doi:10.1029/2007JD008897.

Wang, H., C. Wu, and Y. Wang, 2016: Secondary eyewall formation in an idealized tropical cyclone simulation: Balanced and unbalanced dynamics. *J. Atmos. Sci.*, **73**, 3911–3930, doi:10.1175/JAS-D-15-0146.1.

Wang, X., Y. Ma, and N. E. Davidson, 2013: Secondary eyewall formation and eyewall replacement cycles in a simulated hurricane: Effect of the net radial force in the hurricane boundary layer. *J. Atmos. Sci.*, **70**, 1317–1341, doi:10.1175/JAS-D-12-017.1.

Wang, Y.-Q., 2009: How do outer spiral rainbands affect tropical cyclone structure and intensity? *J. Atmos. Sci.*, **66**, 1250–1273, doi:10.1175/2008JAS2737.1.

Weng, Y.-H., and F. Zhang, 2016: Advances in convection-permitting tropical cyclone analysis and prediction through EnKF assimilation of reconnaissance aircraft observations. *J. Meteor. Soc. Japan*, **94**, 345–358, doi:10.2151/jmsj.2016-018.

Willoughby, H. E., J. A. Clos, and M. G. Shoreibah, 1982: Concentric eye walls, secondary wind maxima, and the evolution of the hurricane vortex. *J. Atmos. Sci.*, **39**, 395–411, doi:10.1175/1520-0469(1982)039<0395:CEWSWM>2.0.CO;2.

Wu, C.-C., Y.-H. Huang, and Z. Tan, 2016: Secondary eyewall formation in tropical cyclones. *Dynamics and Predictability of Large-Scale, High-Impact Weather and Climate Events*, Cambridge University Press, 168–175.

Xu, J., and Y. Wang, 2010: Sensitivity of tropical cyclone inner-core size and intensity to the radial distribution of surface entropy flux. *J. Atmos. Sci.*, **67**, 1831–1852, doi:10.1175/2010JAS3387.1.

Yang, Y. T., H.-C. Kuo, E. A. Hendricks, and M. S. Peng, 2013: Structural and intensity changes of concentric eyewall typhoons in the western North Pacific basin. *Mon. Wea. Rev.*, **141**, 2632–2648, doi:10.1175/MWR-D-12-00251.1.

Zehr, R. M., 2003: Environmental wind shear with Hurricane Bertha. *Wea. Forecasting*, **18**, 345–356, doi:10.1175/1520-0434(2003)018<0345:EVWSWH>2.0.CO;2.

Zhang, F., and Y. Weng, 2015: Predicting hurricane intensity and associated hazards: A five-year real-time forecast experiment with assimilation of airborne Doppler radar observations. *Bull. Amer. Meteor. Soc.*, **96**, 25–33, doi:10.1175/BAMS-D-13-00231.1.

——, D. Tao, Y. Q. Sun, and J. D. Kepert, 2017: Dynamics and predictability of secondary eyewall formation in sheared tropical cyclones. *J. Adv. Model. Earth Syst.*, **9**, 89–112, doi:10.1002/2016MS000729.

Zhou, X., and B. Wang, 2011: Mechanism of concentric eyewall replacement cycles and associated intensity changes. *J. Atmos. Sci.*, **68**, 972–988, doi:10.1175/2011JAS3575.1.

Zhu, Z.-D., and P. Zhu, 2014: The role of outer rainband convection in governing the eyewall replacement cycle in numerical simulations of tropical cyclones. *J. Geophys. Res. Atmos.*, **119**, 8049–8072, doi:10.1002/2014JD021899.